



Less atmospheric radiative heating due to aspherical dust with coarser size

Akinori Ito¹, Adeyemi A. Adebisi², Yue Huang², and Jasper F. Kok²

¹Yokohama Institute for Earth Sciences, JAMSTEC, Yokohama, Kanagawa, 236-0001, Japan.

5 ²Department of Atmospheric and Oceanic Sciences, University of California, Los Angeles, CA 90095, USA.

Correspondence to: Akinori Ito (akinorii@jamstec.go.jp)

Abstract. Mineral dust aerosols cool and warm the atmosphere by scattering and absorbing both solar (short-wave: SW) and thermal (long-wave: LW) radiation. However, large uncertainties remain in dust radiative effects, largely due to differences in the dust size distribution and optical properties simulated in Earth system models. Here, we improve the simulated dust
10 properties with datasets that leverage measurements of size-resolved dust concentration and asphericity factor (improved simulation) in a coupled global chemical transport model (IMPACT) with a radiative transfer module (RRTMG) (default simulation). The global and annual average of dust aerosol optical depth at 550 nm (DAOD₅₅₀) from the improved simulation (0.029) falls within the range of a semi-observation-based estimate (0.030 ± 0.005), in contrast to that (0.023) of the default simulation. Improved agreement against semi-observation-based estimate of the radiative effect efficiency was obtained
15 using less absorptive SW and more absorptive LW dust refractive indices. Our sensitivity simulations reveal that the improved simulation leads to a similar net global dust radiative effect at the Top Of Atmosphere (TOA) on a global scale to the default simulation (-0.08 vs. -0.09 $\text{W}\cdot\text{m}^{-2}$) but results in less cooling at the surface (-0.23 vs. -0.88 $\text{W}\cdot\text{m}^{-2}$), because of enhanced LW warming by coarser aspherical dust. Our results thus suggest less atmospheric radiative heating due to aspherical dust with coarser size over the major source regions (0.15 vs. 0.79 $\text{W}\cdot\text{m}^{-2}$ on a global scale).

20 1 Introduction

Mineral dust aerosols can both cool and warm the climate, but how much dust aerosols net influence global climate is highly uncertain (Penner, 2019). Global dust modeling studies have suggested that mineral dust exerts an aerosol radiative effect (RE) between -0.6 and $+0.2$ $\text{W}\cdot\text{m}^{-2}$ at the Top Of Atmosphere (TOA) and between -0.2 and -2.7 $\text{W}\cdot\text{m}^{-2}$ at the surface (Miller and Tegen, 1998; Balkanski et al., 2007; Tanaka et al., 2007; Takemura et al., 2009; Räisänen et al., 2013; Zhao et al.,
25 2013; Albani et al., 2014; Colarco et al., 2014; Heald et al., 2014; Tuccella et al., 2019; Di Biagio et al., 2020). Whereas a negative RE corresponds to the cooling of the global system when the sunlight is reflected to space, a positive RE corresponds to an overall warming of the atmosphere by trapping incident radiation. The climate feedback does not depend



only on RE at TOA, but also on its difference to the surface value, which represents radiative heating within the atmosphere (Miller et al., 2004; Yoshioka et al., 2007; Lau et al., 2009). The large uncertainties in quantifying the dust RE in the models
30 are mainly propagated from the large spatial heterogeneity and temporal variability of mineral dust abundance and the physicochemical properties (e.g., size distribution, mineral composition, and shape), as well as the ground surface characteristics and atmospheric properties (e.g., surface reflectance, temperature, and atmospheric absorption) (Sicard et al., 2014; Lacagnina et al., 2015; Li and Sokolik, 2018). Below, we provide a brief discussion of the effects of the dust size distribution, mineral composition, and particle shape on dust radiative effects.

35 Recently, there has been increased attention paid to the importance of accurately predicting the abundance of coarse dust for the global energy balance (Kok et al. 2017; Song et al. 2018; Di Biagio et al., 2020; Adebisi and Kok, 2020). The coarser particles are expected to be more prevalent closer to the source regions, as they fall downward much faster than finer particles (Mahowald et al., 2014). For instance, the lifetime of dust aerosols larger than 30 μm in diameter is less than 12 h in most cases except in large haboobs (Ryder et al., 2013). Current models, however, cannot accurately simulate observed
40 transport of coarse dust particles across the Atlantic (Weinzierl et al., 2017; Ansmann et al., 2017), although several hypotheses have been proposed to explain measurements of giant dust particles (larger than 63 μm in diameter) relatively far from source regions (van der Does et al., 2018). For instance, the uplift events of coarse dust can be induced by a nocturnal low-level jet or cold pool outflow from mesoscale convective systems (i.e., haboobs) (Rosenberg, et al. 2014; Ryder et al., 2019). At higher elevation, electrostatic forces and dust asphericity might retard the settling of coarse and giant dust particles
45 and thus may facilitate the transport of these particles over longer distances (Harrison et al., 2018; Toth et al., 2019; Huang et al., 2020a). Other missing processes that affect the transport and deposition of giant particles would also need to be incorporated into the models to reproduce the measurements of the size distribution over the open ocean (van der Does et al., 2018). The coarse dust particles scatter and absorb both the solar (short-wave: SW) and thermal (long-wave: LW) radiation, causing a net warming effect at TOA. In contrast, the fine dust particles principally scatter SW radiation, causing a net
50 cooling effect. Since coarse dust tends to warm the climate, the underestimation of the abundance of coarse dust causes Earth system model to underestimate the warming. On the other hand, model errors due to the underestimated coarse dust load and



corresponding warming might be compensated for in models by using a refractive index that is too absorbing (Di Biagio et al., 2019), and which depends on the mineral composition of the dust.

The dust refractive index is often derived from measurements based on dust or individual mineral particles (Bedidi and Cervelle, 1993; Long et al., 1993; Di Biagio et al., 2017, 2019; Stegmann & Yang, 2017). Indeed, most dust particles are internal mixtures of various mineral compositions and irregular shapes (Reid, 2003; Wiegner et al., 2009; Wagner et al., 2012). In desert soils, iron (Fe) oxides are generally hematite (α -Fe₂O₃) and goethite (FeOOH), which cause soil-derived dust absorption at ultraviolet (UV) and visible wavelengths (Sokolik and Toon, 1999; Balkanski et al., 2007). These two minerals have distinct optical properties which might cause various intensities of shortwave absorption and thus RE of dust aerosols (Lafon et al., 2016). However, the speciation of dust into its mineral components inherently comprises uncertainties on soil mineralogy, Fe content in mineral, and refractive index of Fe oxides, partly due to the differences in prescribed parameters. The atmospheric aging of Fe-containing aerosols can further modulate the optical properties of Fe oxides (Ito et al., 2018), while photochemical transformation of Fe oxides from lithogenic sources due to atmospheric processing is relatively limited (< 10%), compared to pyrogenic sources (Ito et al., 2019).

Previous studies have shown that the assumption of spherical shape in models leads to a substantial underestimation of the extinction efficiency and thus dust aerosol optical depth (DAOD), mainly because the assumption of sphericity causes an underestimation of the surface-to-volume ratio compared to aspherical dust (Kok et al., 2017; Hoshyaripour et al., 2019; Tuccella et al., 2019). Overall, the net radiative effect of dust asphericity on climate simulations is minor on a global scale, partly because the larger DAOD is compensated for by the larger asymmetry parameter of aspherical dust, which reduces the amount of radiation scattered backward to space (Räisänen et al., 2013; Colarco et al., 2014). Moreover, non-spherical calcium-rich dust particles can be converted to spherical particles, due to heterogeneous reactions with nitrate and sulfate on these particles, especially over polluted regions (Laskin et al., 2005; Matsuki et al., 2005). As the plumes move downwind to the oceans, the dust aerosols can be aggregated with sea salt in the marine boundary layer, which leads to more spherical shapes and larger sizes (Zhang and Iwasaka, 2004).

Here, we focus on the influence of the size-resolved abundance of aspherical dust on the aerosol radiative effects in a coupled global chemical transport model (IMPACT) (Ito et al., 2020 and references therein) with a radiative transfer module



(RRTMG) (Iacono et al., 2008) (i.e., default simulation). We improve the accuracy of these simulations by correcting the bias in size-resolved dust concentration with the Dust Constraints from joint Observational-Modelling-Experimental analysis (DustCOMM) data set (Adebisi et al., 2020) (i.e., improved simulation), as well as by considering the aspherical shape (Huang et al., 2020a, 2020b). We then explore the sensitivity to dust refractive index. After evaluating the model outputs against semi-observation-based DAOD at 550 nm (DAOD₅₅₀) and radiative effect efficiencies, the improved simulation suggests much less atmospheric radiative heating over the major source regions, compared to the default simulation (0.15 vs. 0.79 W·m⁻² on a global scale). The term “semi-observation-based” is used for DAOD₅₅₀ and dust radiative effect efficiency when the estimates are based on the combination of observations and models.

85 2 Methods

Since most models underestimate the coarse dust load (Ansmann et al., 2017; Adebisi and Kok, 2020), the sensitivity of dust radiative effects to optical properties in the present study might be considerably different from previous studies. In our study, we regard “fine” and “coarse” dust as dust particles with a diameter less than 2.5 μm (i.e., PM_{2.5}) and between 2.5 and 20 μm, respectively. Here, we examined the dust radiative effects using seven different numerical experiments that varied (1) the simulated dust concentration and their size distribution, (2) particle shape, and (3) mineralogical composition (Tables 1 and 2). Two experiments used the dust concentrations calculated from the forward model with the finer dust size (denoted as “fine”). Subsequently, the simulated dust concentration and the size distribution were adjusted to the semi-observation-based concentrations (Adebisi and Kok, 2020) in the other five experiments with the coarser dust size (denoted as “coarse”). The default simulation used the spherical assumption on the particle shape, whereas the dust asphericity was considered in the other six experiments. We then examined different refractive indices for the dust mineralogy to represent the regional variations in refractive indices (denoted as “region”, “mineral”, or “absorption”). These sensitivity simulations and their radiative effects are summarized in Tables 1 and 2, respectively, with more details below.



2.1 Aerosol chemistry transport model

This study used the Integrated Massively Parallel Atmospheric Chemical Transport (IMPACT) model (Ito et al., 2020 and references therein). Simulations were performed for the year of 2016, using a horizontal resolution of $2.0^{\circ} \times 2.5^{\circ}$ for latitude by longitude and 47 vertical layers. The model used the Modern Era Retrospective analysis for Research and Applications 2 (MERRA-2) reanalysis meteorological data from the National Aeronautics and Space Administration (NASA) Global Modeling and Assimilation Office (GMAO) (Gelaro et al., 2017).

The model simulated the emissions, chemistry, transport, and deposition of major aerosol species, including mineral dust, black carbon (BC), particulate organic matter (POM), sulfate, nitrate, ammonium, and sea spray aerosols, and their precursor gases. Atmospheric processing of mineral dust aerosols, during transport, were projected for four distinct aerosol size bins ($<1.26 \mu\text{m}$, $1.26\text{--}2.5 \mu\text{m}$, $2.5\text{--}5 \mu\text{m}$, and $5\text{--}20 \mu\text{m}$ of diameter). Dust emissions were dynamically simulated using a physically-based emission scheme (Kok et al. 2014; Ito and Kok, 2017) with the soil mineralogical map (Journet et al., 2014; Ito and Shi 2016). The direct emissions of dust are evenly distributed in mixing ratio throughout the planetary boundary layer. The global scaling factor of dust emission was determined from the comparison of the model results with ground-based AOD measurements near the dust source regions prior to the adjustment to the DustCOMM (Kok et al. 2014; Ito and Kok, 2017).

To improve the accuracy of our simulations of mineral dust, we made several upgrades to the on-line emission and gravitational settling schemes used in Ito et al. (2020). The dust emissions were extremely sensitive to soil moisture, and thus the bias was adjusted with satellite observations (Ito and Kok, 2017). However, the satellite measurements were only available every other day depending on location. The Soil Moisture Active Passive (SMAP) Level-4 Soil Moisture data product addressed these limitations by merging the satellite observations into a numerical model of the land surface water and energy balance while considering the uncertainty of the observations and model estimates (Reichle et al., 2019). In this work, we utilized the 3-hourly data of soil moisture derived from the SMAP for barren and open shrublands, separately (Reichle et al., 2018). To achieve this, we used the MODerate resolution Imaging Spectroradiometer (MODIS) land cover map at 500 m resolution to calculate the fraction of barren and open shrublands in each ground surface layer (Friedl et al., 2019)



Compared to the assumption on spherical shapes of aerosols, the dust asphericity increased aerodynamic drag at a given volume and mass, and thus increased gravitational settling lifetime by about 20% (Huang et al., 2020a). Here, we implemented globally averaged asphericity factor of 0.87 (Huang et al., 2020a) to the gravitational settling scheme for mineral dust. Consequently, the lifetime of the dust aerosol for the largest-size bin in the IMPACT model even after accounting for asphericity (1.4 days for 5–20 μm of diameter) was significantly shorter than an ensemble of model results (2.1 \pm 0.3 days for the mass mean diameter of 8.3 μm) (Kok et al., 2017).

2.2 Integration of IMPACT and RRTMG

To improve the accuracy of our simulations of dust RE, we made upgrades to the radiative transfer calculations (Ito et al., 2018). In this study, we integrated the Rapid Radiative Transfer Model for GCMs (RRTMG) online within the IMPACT model to calculate the radiative fluxes associated with atmospheric aerosols. RRTMG is a radiative transfer code that calculates the SW and LW atmospheric fluxes (Iacono et al., 2008). Given the size range of dust particles, scattering and absorption in the on-line model was described in terms of Mie theory. Assuming homogeneous spherical particles, the optical properties such as the mass extinction coefficient, single scattering albedo, and asymmetry parameter were calculated using a look-up table as a function of refractive index and size parameter (Xu and Penner, 2012).

The optical properties from the measurements for dust samples generated from 19 natural soils suggested a considerable role of Fe oxides in determining the SW absorption (Di Biagio et al., 2019). The refractive indices for mineral components were used for hematite, goethite (Bedidi and Cervelle, 1993), silicate particle group, quartz, gypsum (CaSO_4) (Stegmann & Yang, 2017), and calcite (CaCO_3) (Long et al., 1993) in the default simulations (denoted as “mineral”). The hematite and goethite were treated separately according to the mineralogical map (Journet et al., 2014). Consequently, hematite mass content averaged in the dust at emission (0.79% for fine and 0.50% for coarse from the default simulation) was lower than goethite content (1.8% and 1.3%, respectively) on a global scale. In addition to the primary emission of gypsum, CaSO_4 is secondary formed due to the dissolution/precipitation of CaCO_3 in thermodynamic equilibrium condition (Ito and Feng, 2010). For the LW refractive index, we used the global mean of laboratory measurements of the refractive index from 19 natural soils from various source regions around the world (Di Biagio et al., 2017) (denoted as “global”).



As for the SW, the particle size increased with the uptake of sulfate, nitrate, ammonium, and water by the aerosols (Xu and Penner, 2012). These coating materials were treated as internally mixed with dust aerosol in each size bin and thus can reduce solar absorption of mineral dust. As the LW scattering was not accounted for in the RRTMG, we used the adjustment factors of 1.18 ± 0.01 and 2.04 ± 0.18 for the dry particles at the surface and TOA (Dufresne et al., 2002), following Di Biagio et al. (2020) who noted that this adjustment was estimated for dust of diameter less than $10 \mu\text{m}$ and thus might be a lower approximation of the LW scattering by coarse dust. The larger adjustment factor at TOA reflects the fact that the upward LW radiation emitted from the ground surface can be reduced through scattering and absorption, compared to the surface. Subsequently, these optical properties were used by the RRTMG to calculate RE based on dust mixing ratio distributions in the IMPACT model. The dust RE was estimated as the difference in the calculated radiative fluxes with all aerosols and with all aerosols except the dust aerosols for each bin.

The broadband direct and diffuse albedos for both the UV visible and visible IR were specified from the hourly MERRA-2. The surface emissivity was based on the hourly MERRA-2. Long-lived greenhouse gas concentrations were obtained from historical greenhouse gas concentrations for climate models (Meinshausen et al., 2017). Water vapor concentrations were specified according to the MERRA-2. Cloud optical properties were calculated based on the liquid and ice visible optical depths from the MERRA-2, prescribing effective radii of $10 \mu\text{m}$ for water droplets and $25 \mu\text{m}$ for ice particles, respectively (Gettelman et al., 2010; Heald et al., 2014).

2.3 Description of DustCOMM

Dust Constraints from joint Observational-Modelling-experiMental analysis (DustCOMM) is a dataset of three-dimensional (3-D) dust properties obtained by combining observational, experimental, and modeling constraints on dust properties. While details can be found in Adebisi et al. (2020) and Adebisi and Kok (2020), we provide a brief overview here. First, DustCOMM's constraint on the 3-D dust size distribution combines dozens of previously published in-situ measurements of dust size distributions, taken during several field campaigns, with an ensemble of climate model simulations. The framework used those in-situ measurements first to constrain the globally averaged size distribution (Adebisi and Kok, 2020), which is used subsequently to bias adjustment an ensemble of six global model simulations



(Adebisi et al., 2020). The constraints on dust size distribution ranges from 0.2 μm to 20 μm in diameter, where a generalized analytical function describes the sub-bin distribution based on brittle fragmentation theory (Kok, 2011). The second DustCOMM product-atmospheric dust mass loading-combines the constraints on dust size distribution with constraints on dust extinction efficiency and dust aerosol optical depth (Adebisi et al., 2020). The constraints on dust extinction efficiency used the single-scattering database of Meng et al. (2010) and leveraged measurements of the dust index of refraction as well as accounts for the non-spherical shape of dust particles (Kok et al., 2017). For this, we approximate dust as tri-axial ellipsoidal particles described by the globally-representative values of measured dust aspect ratio (the length-to-width ratio) and the height-to-width ratio (HWR) obtained from Huang et al. (2020a). Furthermore, the dust aerosol optical depth used to obtain the dust mass loading combines the semi-observation-based dataset from Ridley et al. (2016) with information from four reanalysis products. This includes the MERRA-2, Navy Aerosol Analysis and Prediction System (NAAPS), Japanese Reanalysis for Aerosol (JRAero), and Copernicus Atmosphere Monitoring Service interim ReAnalysis (CAMSiRA) (Adebisi et al., 2020).

2.4 Description of asphericity factor for optical properties

To account for the dust asphericity, an adjustment factor was applied to the spherical optical properties at each dust size parameter and refractive index. The adjustment factors for the optical properties of non-spherical particles were calculated after Huang et al. (2020b). Specifically, Huang et al. (2020b) combined globally representative dust shape distributions (Huang et al., 2020a) with a shape-resolved single-scattering database (Meng et al., 2010). This database combines four computational methods (Mie theory, T-matrix method, discrete dipole approximation, and an improved geometric optics method) to compute the single-scattering properties of non-spherical dust for a wide range of shape descriptors. Huang et al. (2020b) provided the look-up table containing optical properties of non-spherical dust as functions of size parameter and refractive index.



2.5 Sensitivity simulations

First, the aerosol RE of mineral dust strongly depends on both the magnitude of dust load and the dust size distribution (Tegen and Lacis, 1996; Liao and Seinfeld, 1998). The DustCOMM data set contains total column loading and concentration of mineral dust resolved by season and particle size (Adebisi et al., 2020). To adjust the seasonal dust load in the model, the sum of bin 1, bin 2, and bin 3 dust emission flux was scaled by the seasonal mean of the ratio of the sum of bin 1, bin 2, and bin 3 dust column loading between the model and DustCOMM at each 2-D grid box. When the source function was used for high-latitude dust in the Northern Hemisphere, this led to substantially high emissions and thus RE over there, likely due to the influences from long-range transported dust. Therefore, the direct emissions of dust from the nine major source regions only (Kok et al., 2020) were adjusted using the DustCOMM data (Fig. 1). To adjust the size bias in dust emissions, the mass fraction of emitted dust for each bin was prescribed according to the size-resolved total column loading of DustCOMM at each 2-D grid box. Overall, the IMPACT-simulated lifetime of the dust aerosol for the second-size bin (7.8 days 1.26–2.5 μm of diameter) was in good agreement with the ensemble of model results (8.5 ± 1.1 days for the mass mean diameter of 1.8 μm) (Kok et al., 2017). To maintain the consistency in the DAOD₅₅₀, the mass fraction of dust concentration for each bin between 0.2 and 20.0 μm of diameter were adjusted at each 3-D grid box prior to calculating the radiative fluxes using the RRTMG based on the ratio of mass concentration of PM_{2.5} (i.e., sum of bin 1 and bin 2) to each bin (Table 3).

Second, the approximation of particles to spheres is evaluated applying aspherical factors to the optical properties of the mass extinction coefficient, single scattering albedo, and asymmetry parameter for SW, as well as absorption fraction of extinction for the LW. At the same time, we maintained the consideration of asphericity on the gravitational velocity and kept the dust concentrations unaltered between the spherical (default) and aspherical (fine-global) cases.

Third, the aerosol RE of mineral dust also depends on mineralogical composition. For the sensitivity simulation to refractive index, we used the global mean of laboratory measurements of the refractive index from 19 natural soils from various source regions around the world (Di Biagio et al., 2017, 2019) (denoted as “global”). To investigate the regional heterogeneity of refractive index, regional mean of refractive index was examined (denoted as “region”). The regionally averaged imaginary parts of the refractive indices at wavelength of 0.52 μm and 9.7 μm showed large differences in SW and



LW absorptivity, respectively, between different samples collected at various geographical locations (Fig. 1). The refractive index obtained from 19 samples was aggregated into 9 main source regions and the arithmetic mean was calculated for each source region (Di Biagio et al., 2017, 2019). The global mean was used for other areas. The mineral dust LW refractive index also depends on its mineralogical composition (Sokolik et al., 1998; Di Biagio et al., 2017). The LW refractive index of Volz (1983) has been widely used in climate models and satellite remote sensing algorithms and thus was examined here (denoted as “mineral”). To analyze the dependence of the results on less absorptive SW and more absorptive LW refractive indices, we made further sensitivity simulations by varying the values of imaginary parts of the refractive index within the range of values from Di Biagio et al. (2017, 2019) (10% and 90% percentiles for SW and LW, respectively) (denoted as “absorption”). The associated real parts with the 90% percentile imaginary parts for LW were calculated to account for the Kramers-Kronig relation (Lucarini et al., 2005).

2.6 Semi-observation-based dust SW and LW radiative effect efficiency

Radiative effect efficiency is defined as the gradient of a linear least squares fit applied to the $DAOD_{550}$ and dust radiative effect at each 2-D grid box ($W \cdot m^{-2} DAOD_{550}^{-1}$). To estimate dust radiative effect efficiency, aerosol and radiation remote sensing products have been used with various methods (Table 4) (Zhang and Christopher 2003; Li et al. 2004; Christopher and Jones 2007; Brindley and Russell 2009; Yang et al. 2009; Di Biagio et al. 2010; Hansell et al. 2010; Hansell et al. 2012; Song et al. 2018).

The instantaneous SW radiative effect efficiency at TOA is obtained from the linear regression of TOA radiation flux versus AOD observations, although the values in low-dust periods can be substantially influenced by other types of aerosols such as biomass burning (Li et al. 2004). This radiative effect efficiency corresponds to the instantaneous value derived under the limited condition at the measurements (e.g., solar position, atmospheric condition). From the extrapolation of the instantaneous value, the diurnal mean dust SW radiative effect efficiency at the surface and TOA can be derived based on model calculations.

The LW radiative effect efficiency at TOA can be obtained from the linear regression of TOA radiation flux versus AOD observations over the source regions (Brindley and Russell 2009). However, the observed outgoing longwave radiation



is not only dependent on DAOD but also on other factors such as dust layer height, water vapor content, and other types of aerosols. Thus, the LW radiative effect efficiency is estimated from the difference between observed outgoing longwave radiation and the dust-free outgoing longwave radiation, which can be estimated using radiative transfer model (Song et al., 2018).

245 Consequently, the semi-observation-based estimates of the dust radiative effect efficiency could be biased, in part, due to large uncertainties associated with the estimation method such as spherical assumption on AOD retrieval (Zhou et al., 2020), the selection of cloud-free and dust-dominant data, and dust physicochemical properties. To understand the sensitivity of the dust radiative effect efficiency to the particle size distribution, asphericity, and refractive index of dust, radiative transfer computations have been carried out in previous studies (Li et al., 2004; Song et al., 2018).

250 3. Results and Discussions

We evaluate our results from sensitivity simulations against semi-observation-based estimates of DAOD₅₅₀ and radiative effect efficiency. We focused this evaluation on the North Africa and the North Atlantic in boreal summer (June, July, and August) partly because that was the region and season for which most observational constraints on dust radiative effects were available. The better agreement is obtained for the less absorptive SW (Di Biagio et al., 2019) and the more
255 absorptive LW (Volz, 1983) dust refractive indices with adjustments of size-resolved dust concentration and particle shape. Our improved simulation substantially reduces the model estimates of atmospheric radiative heating due to mineral dust near the major source regions even though it induces only a minor difference in RE at TOA on a global scale, compared to the default simulation.

3.1 Dust load and aerosol optical depth

260 We compared our model estimates of DAOD₅₅₀ against semi-observation-based data (Ridley et al., 2016; Adebisi et al., 2020). Because assuming spherical dust underestimates the mass extinction efficiency by ~30% (Kok et al., 2017), default simulations resulted in a significant underestimation of the global and annual mean of DAOD₅₅₀ (0.023) (Table 3). After considering the dust asphericity for optical properties (fine-global), we adjusted IMPACT-simulated dust loads against dust load constrains of DustCOMM data set. This adjustment led the simulated total dust load to increase from 25 Tg



265 (default) to 32 Tg (improved simulation), which addressed the issue that model underestimated the coarse dust portion (Fig. 2, Table 3). After all, the global and annual mean of DAOD₅₅₀ from the improved simulation (0.029) fell within the range in semi-observation-based estimate (0.030 ± 0.005) (Ridley et al., 2016) (Table 3). We found that the agreement with observations in summer was improved from default to improved simulations, with the correlation coefficients (root mean square errors) increasing (decreasing) from 0.86 (0.08) to 0.91 (0.06), respectively (Fig. 3, Table S1, Fig. S1). We also found 270 improvements in the other three seasons (Table S2). The better agreement suggested that the improved simulation was reasonably constrained by the DAOD₅₅₀ (Ridley et al., 2016; Adebisi et al., 2020).

3.2 Dust SW radiative effect efficiency

Modeled estimates of clear-sky dust SW radiative effect efficiencies ($\text{W}\cdot\text{m}^{-2}\text{ DAOD}_{550}^{-1}$) at the surface (Table S3) and TOA (Table S4) were compared with estimates reported by regional studies based on satellite observations over north 275 Africa and Atlantic (Fig. 4). Comparisons for other regions and seasons were also presented for SW in Fig. S2. Sensitivity simulations demonstrated that the radiative effect efficiency strongly depended on the particle size, refractive index, and particle shape (Fig. 4 and Fig. S3). The adjustment of size-resolved dust concentration and shape with the same refractive index worsened agreement of the SW radiative effect efficiencies against semi-observation-based data for the correlation coefficients (root mean square errors) decreasing (increasing) from 0.96 (17) (from default simulations) to 0.94 (26) (from 280 coarse-mineral) (Fig. S2). Subsequently, the use of less absorptive SW refractive index with the improved simulations led to better agreement for the correlation coefficients (root mean square errors) increasing (decreasing) to 0.95 (22) (from the improved simulation) (Fig. S2). However, the use of much less (10% percentile) absorptive SW refractive index from coarse-absorption simulation (Fig. S2e) deteriorated the agreement at the surface. The differences in the model-based estimates of radiative effect efficiency might arise from different data sets of the refractive index, size distribution, and 285 particle shape (Song et al., 2018).



3.3 Dust LW radiative effect efficiency

Modeled estimates of clear-sky dust LW (Fig. 5) radiative effect efficiencies ($\text{W}\cdot\text{m}^{-2}\text{ DAOD}_{550}^{-1}$) at the surface (Table S5) and TOA (Table S6) were compared with estimates reported by regional studies based on satellite observations over north Africa and Atlantic. Comparisons for other regions and seasons were also presented for LW Fig. S4. Sensitivity simulations demonstrated that the radiative effect efficiency strongly depended on the particle size, refractive index, and particle shape (Fig. 5 and Fig. S5). The improved simulation yielded better agreement with semi-observation-based data, with the correlation coefficients (root mean square errors) increasing (decreasing) from 0.57 (12) (from default simulation) to 0.58 (6.3) (from the improved simulation) (Fig. S4). Substantial differences in dust LW radiative effect efficiencies between the default and the improved simulations were found at the surface over the major source regions. The improved simulation showed better agreements with semi-observation-based estimates of LW radiative effect efficiencies at the surface over tropical Atlantic (21 vs. 24 $\text{W}\cdot\text{m}^{-2}\text{ DAOD}^{-1}$) and China (33 vs. 31–35 $\text{W}\cdot\text{m}^{-2}\text{ DAOD}^{-1}$) compared to the default simulation (8.8 and 22 $\text{W}\cdot\text{m}^{-2}\text{ DAOD}^{-1}$, respectively). The relatively high LW radiative effect efficiencies over western Africa were also consistent with the semi-observation-based data. On the other hand, the relatively low LW radiative effect efficiencies were found over eastern Africa. Moving toward the northeastern side of the region, however, the associated uncertainties in the semi-observation-based values increased (Brindley and Russell 2009).

3.4 Dust radiative effect

The Saharan dust cools the ground surface by reducing the solar radiation reaching the surface and warms the atmosphere by absorbing solar radiation (Fig. 6). On the other hand, thermal emission by dust warms the surface and cools the atmosphere (Fig. 7). Our sensitivity simulations show that annually averaged net instantaneous radiative effect due to mineral aerosol (NET) ranges from -0.38 (coarse-absorption) to $+0.25$ (coarse-mineral) $\text{W}\cdot\text{m}^{-2}$ at TOA (Table 5). Both the default and improved simulations resulted in similar NET RE (-0.09 and -0.08 $\text{W}\cdot\text{m}^{-2}$, respectively) to DustCOMM (-0.11 ± 0.10 $\text{W}\cdot\text{m}^{-2}$). The SW RE by dust outweighs the longwave warming effect at the surface in the default IMPACT simulation (Fig. 8). Consequently, the highly absorbing dust could play an important role in the aerosol radiative forcing for the climate models to alter the West African monsoon, with the radiative heating concentrated in the dust layer (Miller et al.,



310 2004; Lau et al., 2009). Our model results of dust RE from improved simulation, however, suggested much less cooling
($-0.23 \text{ W}\cdot\text{m}^{-2}$) at the surface, compared to the default simulation ($-0.88 \text{ W}\cdot\text{m}^{-2}$), despite similar RE at TOA on a global
scale. Thus, our results demonstrated that the atmospheric radiative heating due to mineral dust was substantially reduced for
the improved simulation ($0.15 \text{ W}\cdot\text{m}^{-2}$), compared to the default simulation ($0.79 \text{ W}\cdot\text{m}^{-2}$). The improved simulation was
obtained from the evaluation against semi-observation-based estimates of DAOD₅₅₀, SW and LW radiative effect
315 efficiencies.

To investigate the differences in dust radiative effects between the default and improved simulations, the differences
in annually averaged radiative effects of mineral dust from coarse-global simulation were shown in Fig. 9. A slope of one in
Fig. 9 represented an identical change in both the surface and TOA, and thus corresponded to no change in radiative heating
within the atmosphere. The distances from the coarse-global simulation demonstrated that the large uncertainties existed for
320 the size distribution and refractive index. Our sensitivity simulations revealed that the improved simulation led to a similar
enhancement of NET RE at TOA to the default simulation ($+0.12$ vs. $+0.11 \text{ W}\cdot\text{m}^{-2}$ at the vertical axis of red star and black
star, respectively, in Fig. 9c) but results in less cooling at the surface ($+0.42$ vs. $-0.20 \text{ W}\cdot\text{m}^{-2}$ at the horizontal axis in Fig.
9c). This revision can be divided into (1) the size-resolved abundance for both SW and LW (black triangles in Fig. 9a and
Fig. 9b, respectively), (2) mineralogical variability for SW (red diamonds in Fig. 9a) and for LW (red diamonds in Fig. 9b),
325 and (3) particle shape.

First, at TOA, the SW RE was more sensitive to the size-resolved abundance ($-0.17 \text{ W}\cdot\text{m}^{-2}$ at the vertical axis of
black triangle in Fig. 9a), compared to LW ($0.01 \text{ W}\cdot\text{m}^{-2}$ at the vertical axis of black triangle in Fig. 9b) (Liao and Seinfeld,
1998). Second, this less SW cooling effect with coarser dust was partially compensated for by more SW cooling by the less
absorptive SW refractive index ($0.33 \text{ W}\cdot\text{m}^{-2}$ at the vertical axis of red diamond in Fig. 9a). Thirdly, the sensitivity of SW RE
330 to dust asphericity was rather minor, partly because the lower DAOD was compensated for by the lower asymmetry
parameter of spherical dust, which enhanced the amount of radiation scattered backward to space (Räsänen et al., 2013;
Colarco et al., 2014). The partial compensation led to a small enhancement of SW RE for the default simulation ($0.13 \text{ W}\cdot\text{m}^{-2}$
at the vertical axis of black star in Fig. 9a) and thus the resulting NET RE.



In contrast, at the surface, our sensitivity simulations demonstrated substantially different responses in the RE, mostly
335 because of LW warming effects (+0.42 vs. $-0.20 \text{ W}\cdot\text{m}^{-2}$ at the horizontal axis in Fig. 9b). The enhanced SW cooling by the
more absorbing dust ($-0.38 \text{ W}\cdot\text{m}^{-2}$ at the horizontal axis of red diamond in Fig. 9a) was mostly compensated for by the
reduced SW cooling with coarser dust ($0.12 \text{ W}\cdot\text{m}^{-2}$ at the horizontal axis of black triangle in Fig. 9a) and asphericity. This
led to minor change in SW cooling by the default simulation ($-0.03 \text{ W}\cdot\text{m}^{-2}$ at the horizontal axis of black star in Fig. 9a). In
contrast, enhanced LW warming by more absorptive LW refractive index ($+0.42 \text{ W}\cdot\text{m}^{-2}$ at the horizontal axis of red
340 diamond in Fig. 9b) was accompanied with enhanced LW warming by the coarser dust ($0.07 \text{ W}\cdot\text{m}^{-2}$ at the horizontal axis of
black triangle in Fig. 9b) and asphericity ($0.13 \text{ W}\cdot\text{m}^{-2}$ from the difference between black triangle and black star in Fig. 9b).
As a result, our sensitivity simulations revealed the reduced radiative heating within the atmosphere (less than the dashed
line of red star in Fig. 9c) by the improved simulation ($-0.30 \text{ W}\cdot\text{m}^{-2}$), compared to the enhanced radiative heating (more than
the dashed line of black star in Fig. 9c) by default simulation ($0.34 \text{ W}\cdot\text{m}^{-2}$).

345 4. Conclusions

Accurate estimates of the size-resolved dust abundance, their optical properties, and their seasonality in regional and
vertical scales provides a step towards a more reliable projection of the climatic feedback of mineral aerosols. The radiative
effect efficiency depends on numerous variables in model simulations, including the spatial distribution and temporal
variation of size-resolved dust concentrations, the mass extinction coefficient, single scattering albedo, and asymmetry
350 parameter of dust. Since the models typically underestimate the coarse dust load, the sensitivity to the aerosol absorptivity
might be considerably different from previous studies. Thus, the model results should be re-evaluated against semi-
observation-based estimate of the radiative effect efficiency.

We improved the accuracy of the simulations by adjusting the bias in size-resolved aspherical dust concentration with
the DustCOMM data set. Alternatively, dust mineralogy might contribute to the underestimates of modeled aerosol
355 absorption compared to satellite observations (Lacagnina, et al. 2015). This enhanced aerosol absorption was examined by
specifying the mineralogy with varying amounts of light-absorbing Fe oxides for SW. The better agreement with the semi-
observation-based data of dust radiative effect efficiency was obtained using the less absorptive SW and the more absorptive
LW dust refractive indices after the adjustments of dust sizes and shapes. The improved simulation led to similar net global



dust radiative effect at TOA on a global scale to the default simulation (-0.08 vs. -0.09 $\text{W}\cdot\text{m}^{-2}$) but results in less cooling at
360 the surface (-0.23 vs. -0.88 $\text{W}\cdot\text{m}^{-2}$). Consequently, the atmospheric heating due to mineral dust was substantially reduced
for the improved simulation (0.15 $\text{W}\cdot\text{m}^{-2}$), compared to the intensified atmospheric heating from the default IMPACT
simulation (0.79 $\text{W}\cdot\text{m}^{-2}$). The less intensified atmospheric heating due to mineral dust could substantially modify vertical
temperature profile in Earth system models, and thus has important implications for the projection of dust feedback near the
major source regions in past and future climate changes (Kok et al., 2018). More accurate semi-observation-based dust SW
365 and LW radiative effect efficiency over strong dust source regions are needed to narrow the uncertainty in the RE.

Currently, the model did not include dust particles above 20 μm , but a substantial fraction of airborne dust near
source regions may be above this threshold (Ryder et al., 2019). The giant dust is likely important for the radiative effects, as
well as for biogeochemical effects in the North Atlantic (Pabortsava et al., 2017; van der Does et al., 2018). In such an
extreme case as the “Godzilla” dust storm over North Africa in June 2020 (Francis et al., 2020), the dust loading could be
370 larger than that examined for this study, and our estimates of the warming effects might be conservative during such events.
However, to keep the giant particles in the atmosphere, the modeled deposition fluxes should be reduced from the current
model. Therefore, models should improve their ability to capture the evolution of the dust size distribution as the plumes
move downwind of the source regions.

Code availability.

375 The source code of the RRTMG have been obtained from the web site at https://github.com/AER-RC/RRTMG_LW and
https://github.com/AER-RC/RRTMG_SW. The source code of the Kramers-Kronig relations have been obtained from the
web site at [https://www.mathworks.com/matlabcentral/fileexchange/8135-tools-for-data-analysis-in-optics-acoustics-signal-](https://www.mathworks.com/matlabcentral/fileexchange/8135-tools-for-data-analysis-in-optics-acoustics-signal-processing)
processing.

Data availability.

380 SMAP data have been obtained from the web site at <https://nsidc.org/data/smap/smap-data.html>. MODIS land data have
been retrieved from the web site at <https://ladsweb.modaps.eosdis.nasa.gov/>. MERRA-2 data have been provided by the



Global Modeling and Assimilation Office (GMAO) at NASA Goddard Space Flight Center (<https://disc.gsfc.nasa.gov/datasets/>). The DustCOMM data are available at <https://dustcomm.atmos.ucla.edu/>. The datasets supporting the conclusions of this article are included within the article and its supplement file.

385 **Supplement.**

The supplement related to this article is available online at:

Author contributions.

AI and JFK initiated the modeling collaboration with semi-observation-based data sets. AI carried out the modeling study. AAA, YH, JFK contributed semi-observation-based data sets of DustCOMM and asphericity factor. All authors read and
390 approved the final manuscript.

Competing interests.

The authors declare that they have no competing interest.

Acknowledgements.

Numerical simulations were performed using the Hewlett Packard Enterprise (HPE) Apollo at the Japan Agency for Marine-
395 Earth Science and Technology (JAMSTEC).

Financial support.

Support for this research was provided to A.I. by JSPS KAKENHI Grant Number 20H04329 and 18H04143, and Integrated Research Program for Advancing Climate Models (TOUGOU) Grant Number JPMXD0717935715 from the Ministry of Education, Culture, Sports, Science and Technology (MEXT), Japan. This work was developed with support from the
400 University of California President's Postdoctoral Fellowship awarded to A.A.A., and from the National Science Foundation



(NSF) grants 1552519 and 1856389 awarded to J.F.K. Y.H. acknowledges support from NASA grant 80NSSC19K1346, awarded under the Future Investigators in NASA Earth and Space Science and Technology (FINESST) program.

Review statement.

This paper was edited by and reviewed by referees.

405 **References**

- Adebisi, A. A., Kok, J. F., Wang, Y., Ito, A., Ridley, D. A., Nabat, P., and Zhao, C.: Dust Constraints from joint Observational-Modelling-experiMental analysis (DustCOMM): comparison with measurements and model simulations, *Atmos. Chem. Phys.*, 20, 829–863, <https://doi.org/10.5194/acp-20-829-2020>, 2020.
- Adebisi, A. A. and Kok, J. F.: Climate models miss most of the coarse dust in the atmosphere, *Sci. Adv.*, 6, eaaz9507, <https://doi.org/10.1126/sciadv.aaz9507>, 2020.
- 410 Albani, S., Mahowald, N. M., Perry, A. T., Scanza, R. A., Heavens, N. G., Zender, C. S., Maggi, V., Kok, J. F., and Otto-Bliesner, B. L.: Improved dust representation in the Community Atmosphere Model. *J. Adv. Model. Earth Syst.*, 6, 541–570, <https://doi.org/10.1002/2013MS000279>, 2014.
- Ansmann, A., Rittmeister, F., Engelmann, R., Basart, S., Jorba, O., Spyrou, C., Remy, S., Skupin, A., Baars, H., Seifert, P.,
415 Senf, F., and Kanitz, T.: Profiling of Saharan dust from the Caribbean to western Africa – Part 2: Shipborne lidar measurements versus forecasts, *Atmos. Chem. Phys.*, 17, 14987–15006, <https://doi.org/10.5194/acp-17-14987-2017>, 2017.
- Balkanski, Y., Schulz, M., Claquin, T., and Guibert, S.: Reevaluation of Mineral aerosol radiative forcings suggests a better agreement with satellite and AERONET data, *Atmos. Chem. Phys.*, 7, 81–95, [https://doi.org/10.5194/acp-7-81-](https://doi.org/10.5194/acp-7-81-2007)
420 2007, 2007.
- Bedidi, A. and Cervelle, B.: Light scattering by spherical particles with hematite and goethitelike optical properties: effect of water impregnation, *J. Geophys. Res.*, 98, 11941–11952, 1993, <https://doi.org/10.1029/93JB00188>.



- 425 Brindley, H. E. and Russell, J. E.: An assessment of Saharan dust loading and the corresponding cloud-free longwave direct radiative effect from geostationary satellite observations, *J. Geophys. Res.-Atmos.*, 114, D23201, 2009, <https://doi.org/10.1029/2008jd011635>.
- Colarco, P. R., Nowottnick, E. P., Randles, C. A., Yi, B. Q., Yang, P., Kim, K. M., Smith, J. A., and Bardeen, C. G.: Impact of radiatively interactive dust aerosols in the NASA GEOS-5 climate model: Sensitivity to dust particle shape and refractive index, *J. Geophys. Res.-Atmos.*, 119, 753–786, 2014, <https://doi.org/10.1002/2013JD020046>.
- 430 Christopher, S. A. and Jones, T.: Satellite-based assessment of cloud-free net radiative effect of dust aerosols over the Atlantic Ocean, *Geophys. Res. Lett.*, 34, L02810, 2007, doi:10.1029/2006GL027783.
- Di Biagio, C., di Sarra, A., and Meloni, D.: Large atmospheric shortwave radiative forcing by Mediterranean aerosol derived from simultaneous ground-based and spaceborne observations, and dependence on the aerosol type and single scattering albedo, *J. Geophys. Res.*, 115, D10209, 2010, <https://doi.org/10.1029/2009JD012697>.
- 435 Di Biagio, C., Formenti, P., Balkanski, Y., Caponi, L., Cazaunau, M., Panguì, E., Journet, E., Nowak, S., Caquineau, S., Andreae, M. O., Kandler, K., Saeed, T., Piketh, S., Seibert, D., Williams, E., and Doussin, J.-F.: Global scale variability of the mineral dust long-wave refractive index: a new dataset of in situ measurements for climate modeling and remote sensing, *Atmos. Chem. Phys.*, 17, 1901–1929, 2017, <https://doi.org/10.5194/acp-17-1901-2017>.
- 440 Di Biagio, C., Formenti, P., Balkanski, Y., Caponi, L., Cazaunau, M., Panguì, E., Journet, E., Nowak, S., Andreae, M. O., Kandler, K., Saeed, T., Piketh, S., Seibert, D., Williams, E., and Doussin, J.-F.: Complex refractive indices and single-scattering albedo of global dust aerosols in the shortwave spectrum and relationship to size and iron content, *Atmos. Chem. Phys.*, 19, 15503–15531, 2019, <https://doi.org/10.5194/acp-19-15503-2019>.
- 445 Di Biagio, C., Balkanski, Y., Albani, S., Boucher, O., and Formenti, P.: Direct radiative effect by mineral dust aerosols constrained by new microphysical and spectral optical data. *Geophys. Res. Lett.*, 47, e2019GL086186, 2020, <https://doi.org/10.1029/2019GL086186>
- Dufresne, J., Gautier, C., Ricchizzi, P., and Fouquart, Y.: Longwave scattering effects of mineral aerosols, *J. Atmos. Sci.*, 59(12), 1959–1966, 2002, [https://doi.org/10.1175/1520-0469\(2002\)059<1959:LSEOMA>2.0.CO;2](https://doi.org/10.1175/1520-0469(2002)059<1959:LSEOMA>2.0.CO;2).



- Francis, D., Fonseca, R., Nelli, N., Cuesta, J., Weston, M., Evan, A., and Temimi, M.: The atmospheric drivers of the major Saharan dust storm in June 2020. *Geophys. Res. Lett.*, 47, e2020GL090102, 2020, 450 <https://doi.org/10.1029/2020GL090102>.
- Friedl, M., and Sulla-Menashe, D.: MCD12Q1 MODIS/Terra+Aqua Land Cover Type Yearly L3 Global 500m SIN Grid V006 [Data set]. NASA EOSDIS Land Processes DAAC, 2019, <https://doi.org/10.5067/MODIS/MCD12Q1.006>
- Gelaro, R., McCarty, W., Suárez, M. J., Todling, R., Molod, A., Takacs, L., Randles, C. A., Darmenov, A., Bosilovich, M. G., Reichle, R., Wargan, K., Coy, L., Cullather, R., Draper, C., Akella, S., Buchard, V., Conaty, A., da Silva, A. M., 455 Gu, W., Kim, G.-K., Koster, R., Lucchesi, R., Merkova, D., Nielsen, J. E., Partyka, G., Pawson, S., Putman, W., Rienecker, M., Schubert, S. D., Sienkiewicz, M., and Zhao, B.: The Modern-Era Retrospective Analysis for Research and Applications, Version 2 (MERRA-2), *J. Climate*, 30, 5419–5454, 2017, <https://doi.org/10.1175/JCLI-D-16-0758.1>.
- Gottelman, A., Liu, X., Ghan, S. J., Morrison, H., Park, S., Conley, A. J., Klein, S. A., Boyle, J., Mitchell, D. L., and Li, J. L. 460 F.: Global simulations of ice nucleation and ice supersaturation with an improved cloud scheme in the Community Atmosphere Model, *J. Geophys. Res.*, 115, D18216, 2010, <https://doi.org/10.1029/2009jd013797>.
- Harrison, R. G., Nicoll, K. A., Marlton, G. J., Ryder, C. L., and Bennett, A. J.: Saharan dust plume charging observed over the UK, *Environ. Res. Lett.*, 13, 054018, <https://doi.org/10.1088/1748-9326/aabcd9>, 2018.
- Hansell, R. A., Tsay, S., Hsu, N. C., Ji, Q., Bell, S. W., Brent, N. H., Welton, E. J., Roush, T. L., Zhang, W., Huang, J., Li Z. 465 Q., and Chen, H.: An assessment of the surface longwave direct radiative effect of airborne dust in Zhangye, China, during the Asian Monsoon Years field experiment (2008), *J. Geophys. Res.*, 117, D00K39, 2012, <https://doi.org/10.1029/2011JD017370>.
- Hansell, R. A., Tsay, S. C., Ji, Q., Hsu, N. C., Jeong, M. J., Wang, S. H., Reid, J. S., Liou, K. N., and Ou, S. C.: An 470 assessment of the surface longwave direct radiative effect of airborne saharan dust during the NAMMA field campaign, *J. Atmos. Sci.* 67, 1048–1065, 2010, doi:10.1175/2009JAS3257.1.



- Heald, C. L., Ridley, D. A., Kroll, J. H., Barrett, S. R. H., Cady-Pereira, K. E., Alvarado, M. J., and Holmes, C. D.:
Contrasting the direct radiative effect and direct radiative forcing of aerosols, *Atmos. Chem. Phys.*, 14, 5513–5527,
2014, <https://doi.org/10.5194/acp-14-5513-2014>.
- Huang, Y., Kok, J. F., Kandler, K., Lindqvist, H., Nousiainen, T., Sakai, T., Adebisi, A., and Jokinen, O.: Climate Models
and Remote Sensing Retrievals Neglect Substantial Desert Dust Asphericity, *Geophys. Res. Lett.*, 47,
475 e2019GL086592, 2020a, <https://doi.org/10.1029/2019GL086592>.
- Huang, Y., Adebisi, A. & Kok, J. 2020b, Linking the different diameter types of aspherical desert dust indicates that models
underestimate coarse dust emission, American Geophysical Union, Fall Meeting 2020, abstract A007-0016, doi:
10.1002/essoar.10504925.1.
- 480 Hoshyaripour, G. A., Bachmann, V., Förstner, J., Steiner, A., Vogel, H., Wagner, F., Walter, C., and Vogel, B.: Effects of
Particle Nonsphericity on Dust Optical Properties in a Forecast System: Implications for Model-Observation
Comparison, *J. Geophys. Res.-Atmos.*, 124, 2018JD030228, 2019, <https://doi.org/10.1029/2018JD030228>.
- Iacono, M. J., Delamere, J. S., Mlawer, E. J., Shephard, M. W., Clough, S. A., and Collins, W. D.: Radiative forcing by long-
lived greenhouse gases: Calculations with the AER radiative transfer models, *J. Geophys. Res.*, 113, D13103, 2008,
485 <https://doi.org/10.1029/2008JD009944>.
- Ito, A. and Feng, Y.: Role of dust alkalinity in acid mobilization of iron, *Atmos. Chem. Phys.*, 10, 9237–9250, 2010,
<https://doi.org/10.5194/acp-10-9237-2010>.
- Ito, A. and Shi, Z.: Delivery of anthropogenic bioavailable iron from mineral dust and combustion aerosols to the ocean,
Atmos. Chem. Phys., 16, 85–99, 2016, <https://doi.org/10.5194/acp-16-85-2016>.
- 490 Ito, A. and Kok, J. F.: Do dust emissions from sparsely vegetated regions dominate atmospheric iron supply to the Southern
Ocean?, *J. Geophys. Res.-Atmos.*, 122, 3987–4002, 2017, <https://doi.org/10.1002/2016JD025939>.
- Ito, A., Lin, G., and Penner, J. E.: Radiative forcing by lightabsorbing aerosols of pyrogenetic iron oxides, *Sci. Rep.-UK*, 8,
7347, 2018, <https://doi.org/10.1038/s41598-018-25756-3>.
- Ito, A., Myriokefalitakis, S., Kanakidou, M., Mahowald, N. M., Scanza, R. A., Hamilton, D. S., Baker, A. R., Jickells, T.,
495 Sarin, M., Bikkina, S., Gao, Y., Shelley, R. U., Buck, C. S., Landing, W. M., Bowie, A. R., Perron, M. M. G.,



- Guieu, C., Meskhidze, N., Johnson, M. S., Feng, Y., Kok, J. F., Nenes, A., and Duce, R. A.: Pyrogenic iron: The missing link to high iron solubility in aerosols, *Sci. Adv.*, 5, eaau7671, 2019, <https://doi.org/10.1126/sciadv.aau7671>.
- 500 Ito, A., Perron, M. M. G., Proemse, B. C., Strzelec, M., Gault-Ringold, M., Boyd, P. W. and Bowie, A. R.: Evaluation of aerosol iron solubility over Australian coastal regions based on inverse modeling: implications of bushfires on bioaccessible iron concentrations in the Southern Hemisphere, *Prog. Earth Planet. Sci.*, 7, 42, 2020, <https://doi.org/10.1186/s40645-020-00357-9>.
- Journet, E., Balkanski, Y., and Harrison, S. P.: A new data set of soil mineralogy for dust-cycle modeling, *Atmos. Chem. Phys.*, 14, 3801–3816, 2014, <https://doi.org/10.5194/acp-14-3801-2014>.
- 505 Kok, J. F.: A scaling theory for the size distribution of emitted dust aerosols suggests climate models underestimate the size of the global dust cycle, *P. Natl. Acad. Sci. USA*, 108, 1016–1021, 2011, <https://doi.org/10.1073/pnas.1014798108>.
- Kok, J. F., Parteli, E. J. R., Michaels, T. I., and Karam, D. B.: The physics of wind-blown sand and dust, *Rep. Prog. Phys.*, 75, 106901, 2012, doi:10.1088/0034-4885/75/10/106901.
- Kok, J. F., Mahowald, N. M., Fratini, G., Gillies, J. A., Ishizuka, M., Leys, J. F., Mikami, M., Park, M.-S., Park, S.-U., Van 510 Pelt, R. S., and Zobeck, T. M.: An improved dust emission model – Part 1: Model description and comparison against measurements, *Atmos. Chem. Phys.*, 14, 13023–13041, 2014, <https://doi.org/10.5194/acp-14-13023-2014>.
- Kok, J. F., Ridley, D. A., Zhou, Q., Miller, R. L., Zhao, C., Heald, C. L., Ward, D. S., Albani, S., and Haustein, K.: Smaller desert dust cooling effect estimated from analysis of dust size and abundance, *Nat. Geosci.*, 10, 274–278, 2017, <https://doi.org/10.1038/ngeo2912>.
- 515 Kok, J. F., Ward, D. S., Mahowald, N. M., and Evan, A. T.: Global and regional importance of the direct dust-climate feedback, *Nat. Commun.*, 9, 241, 2018, <https://doi.org/10.1038/s41467-017-02620-y>.
- Kok, J. F., Adebisi, A. A., Albani, S., Balkanski, Y., Checa-Garcia, R., Chin, M., Colarco, P. R., Hamilton, D. S., Huang, Y., Ito, A., Klose, M., Leung, D. M., Li, L., Mahowald, N. M., Miller, R. L., Obiso, V., Pérez García-Pando, C., Rocha-Lima, A., Wan, J. S., and Whicker, C. A.: Improved representation of the global dust cycle using observational



- 520 constraints on dust properties and abundance, *Atmos. Chem. Phys. Discuss.*, <https://doi.org/10.5194/acp-2020-1131>,
in review, 2020.
- Lacagnina, C., Hasekamp, O. P., Bian, H., Curci, G., Myhre, G., van Noije, T., Schulz, M., Skeie, R. B., Takemura, T., and
Zhang, K.: Aerosol single-scattering albedo over the global oceans: Comparing PARASOL retrievals with
AERONET, OMI, and AeroCom models estimates, *J. Geophys. Res.*, 120, 9814–9836, 2015,
525 <https://doi.org/10.1002/2015JD023501>.
- Laskin, A., Iedema, M. J., Ichkovich, A., Graber, E. R., Taraniukb, I., and Yinon, R.: Direct observation of completely
processed calcium carbonate dust particles, *Faraday Discuss.*, 130, 453–468, 2005,
<https://doi.org/10.1039/B417366J>.
- Lau, K. M., Kim, K. M., Sud, Y. C., and Walker, G. K.: A GCM study of the response of the atmospheric water cycle of
530 West Africa and the Atlantic to Saharan dust radiative forcing, *Ann. Geophys.*, 27, 4023–4037, 2009,
<https://doi.org/10.5194/angeo-27-4023-2009>.
- Li, F., Vogelmann, A. M., and Ramanathan, V.: Dust aerosol radiative forcing measured from space over the Western Africa,
J. Climate, 17(13), 2558–2571, 2004, [https://doi.org/10.1175/1520-0442\(2004\)017<2558:SDARFM>2.0.CO;2](https://doi.org/10.1175/1520-0442(2004)017<2558:SDARFM>2.0.CO;2)
- Li, L., and Sokolik, I. N.: The dust direct radiative impact and its sensitivity to the land surface state and key minerals in the
535 WRF-Chem-DuMo model: A case study of dust storms in Central Asia, *J. Geophys. Res.-Atmos.*, 123, 4564–4582,
2018, <https://doi.org/10.1029/2017JD027667>
- Liao, H. and Seinfeld, J.: Radiative forcing by mineral dust aerosols: sensitivity to key variables, *J. Geophys. Res.*, 103,
31637–31645, 1998, <https://doi.org/10.1029/1998JD200036>.
- Long, L. L., Query, M. R., Bell, R. J., and Alexander, R. W.: Optical properties of calcite and gypsum in crystalline and
540 powdered form in the infrared and far-infrared, *Infrared Phys.*, 34, 191–201, 1993, [https://doi.org/10.1016/0020-0891\(93\)90008-U](https://doi.org/10.1016/0020-0891(93)90008-U).
- Lucarini, V., Saarinen, J. J., Peiponen, K.-E., and Vartiainen, E. M.: *Kramers-Kronig relations in optical materials research*,
vol. 110, Switzerland: Springer Science & Business Media, 2005.



- 545 Mahowald, N., Albani, S., Kok, J. F., Engelstaeder, S., Scanza, R., Ward, D. S., and Flanner, M. G.: The size distribution of
desert dust aerosols and its impact on the Earth system, *Aeolian Res.*, 15, 53–71, 2014,
<https://doi.org/10.1016/j.aeolia.2013.09.002>, 2014.
- Matsuki, A., Iwasaka, Y., Shi, G., Zhang, D., Trochkin, D., Yamada, M., Kim, Y.-S., Chen, B., Nagatani, T., Miyazawa, T.,
Nagatani, M., and Nakata, H.: Morphological and chemical modification of mineral dust: Observational insight into
the heterogeneous uptake of acidic gases, *Geophys. Res. Lett.*, 32, L22806, 2005,
550 <https://doi.org/10.1029/2005gl024176>.
- Meinshausen, M., Vogel, E., Nauels, A., Lorbacher, K., Meinshausen, N., Etheridge, D. M., Fraser, P. J., Montzka, S. A.,
Rayner, P. J., Trudinger, C. M., Krummel, P. B., Beyerle, U., Canadell, J. G., Daniel, J. S., Enting, I. G., Law, R.
M., Lunder, C. R., O'Doherty, S., Prinn, R. G., Reimann, S., Rubino, M., Velders, G. J. M., Vollmer, M. K., Wang,
R. H. J., and Weiss, R.: Historical greenhouse gas concentrations for climate modelling (CMIP6), *Geosci. Model*
555 *Dev.*, 10, 2057–2116, 2017, <https://doi.org/10.5194/gmd-10-2057-2017>.
- Meng, Z., Yang, P., Kattawar, G. W., Bi, L., Liou, K. N., and Laszlo, I.: Single-scattering properties of tri-axial ellipsoidal
mineral dust aerosols: a database for application to radiative transfer calculations, *J. Aerosol Sci.*, 41, 501–512,
2010, <https://doi.org/10.1016/j.jaerosci.2010.02.008>.
- Miller, R. L. and Tegen, I.: Climate response to soil dust aerosols, *J. Climate*, 11, 3247–3267, 1998,
560 [https://doi.org/10.1175/1520-0442\(1998\)011<3247:CRTSDA>2.0.CO;2](https://doi.org/10.1175/1520-0442(1998)011<3247:CRTSDA>2.0.CO;2).
- Miller, R. L., Tegen, I., and Perlwitz, J.: Surface radiative forcing by soil dust aerosols and the hydrologic cycle, *J. Geophys.*
Res., 109, D04203, 2004, <https://doi.org/10.1029/2003JD004085>.
- Pabortsava, K., Lampitt, R. S., Benson, J., Crowe, C., McLachlan, R., Le Moigne, F. A. C., Mark Moore, C., Pebody, C.,
Provost, P., Rees, A. P., Tilstone, G. H., and Woodward, E. M. S.: Carbon sequestration in the deep Atlantic
565 enhanced by Saharan dust. *Nat. Geosci.* 10, 189–194, 2017, <https://doi.org/10.1038/ngeo2899>.
- Penner, J.: Soot, sulfate, dust and the climate—Three ways through the fog. *Nature*, 570, 158–159, 2019,
<https://doi.org/10.1038/d41586-019-01791-6>.



- Räisänen, P., Haapanala, P., Chung, C. E., Kahnert, M., Makkonen, R., Tonttila, J., and Nousiainen, T.: Impact of dust particle nonsphericity on climate simulations, *Q. J. Roy. Meteor. Soc.*, 139, 2222–2232, 2013, <https://doi.org/10.1002/qj.2084>.
570
- Reichle, R. H., de Lannoy, G., Koster, R. D., Crow, W. T., Kimball, J. S., and Liu, Q.: SMAP L4 global 3-hourly 9 km EASE-grid surface and root zone soil moisture geophysical data, version 4. NASA National Snow and Ice Data Center Distributed Active Archive Center, 2018, <https://doi.org/10.5067/kpjnn2gi1dqr>.
- Reichle, R. H., Liu, Q., Koster, R. D., Crow, W. T., De Lannoy, G. J. M., Kimball, J. S., Ardizzone, J. V., Bosch, D., Colliander, A., Cosh, M., Kolassa, J., Mahanama, S. P., Prueger, J., Starks, P., and Walker, J. P.: Version 4 of the SMAP Level-4 Soil Moisture algorithm and data product. *J. Adv. Model Earth Syst.*, 11, 3106–3130, 2019, <https://doi.org/10.1029/2019MS001729>.
575
- Reid, E. A., Reid, J. S., Meier, M. M., Dunlap, M. R., Cliff, S. S., Broumas, A., Perry, K., and Maring, H.: Characterization of African dust transported to Puerto Rico by individual particle and size segregated bulk analysis, *J. Geophys. Res.*, 108, 8591, 2003, <https://doi.org/10.1029/2002JD002935>, D19.
580
- Ridley, D. A., Heald, C. L., Kok, J. F., and Zhao, C.: An observationally constrained estimate of global dust aerosol optical depth, *Atmos. Chem. Phys.*, 16, 15097–15117, 2016, <https://doi.org/10.5194/acp-16-15097-2016>.
- Rosenberg, P. D., Parker, D. J., Ryder, C. L., Marsham, J. H., Garcia-Carreras, L., Dorsey, J. R., Brooks, I. M., Dean, A. R., Crosier, J., McQuaid, J. B., and Washington, R.: Quantifying particle size and turbulent scale dependence of dust flux in the Sahara using aircraft measurements, *J. Geophys. Res.-Atmos.*, 119, 7577–7598, 2014, <https://doi.org/10.1002/2013JD021255>.
585
- Ryder, C. L., Highwood, E. J., Lai, T. M., Sodemann, H., and Marsham, J. H.: Impact of atmospheric transport on the evolution of microphysical and optical properties of Saharan dust, *Geophys. Res. Lett.*, 40, 2433–2438, 2013, <https://doi.org/10.1002/grl.50482>.
- Ryder, C. L., Highwood, E. J., Walser, A., Seibert, P., Philipp, A., and Weinzierl, B.: Coarse and giant particles are ubiquitous in Saharan dust export regions and are radiatively significant over the Sahara, *Atmos. Chem. Phys.*, 19, 15353–15376, 2019, <https://doi.org/10.5194/acp-19-15353-2019>.
590



- Sicard, M., Bertolín, S., Mallet, M., Dubuisson, P., and Comerón, A.: Estimation of mineral dust long-wave radiative forcing: sensitivity study to particle properties and application to real cases in the region of Barcelona, *Atmos. Chem. Phys.*, 14, 9213–9231, 2014, <https://doi.org/10.5194/acp-14-9213-2014>.
595
- Sokolik, I. N., Toon, O. B., and Bergstrom, R. W.: Modeling the radiative characteristics of airborne mineral aerosols at infrared wavelengths, *J. Geophys. Res.*, 103, 8813–8826, 1998, <https://doi.org/10.1029/98JD00049>.
- Sokolik, I. N. and Toon, O. B.: Incorporation of mineralogical composition into models of the radiative properties of mineral aerosol from UV to IR wavelengths, *J. Geophys. Res.*, 104(D8), 9423–9444, 1999,
600 <https://doi.org/10.1029/1998JD200048>.
- Song, Q., Zhang, Z., Yu, H., Kato, S., Yang, P., Colarco, P., Remer, L. A., and Ryder, C. L.: Net radiative effects of dust in the tropical North Atlantic based on integrated satellite observations and in situ measurements, *Atmos. Chem. Phys.*, 18, 11303–11322, 2018, <https://doi.org/10.5194/acp-18-11303-2018>.
- Stegmann, P. G. and Yang, P.: A regional, size-dependent, and causal effective medium model for Asian and Saharan
605 mineral dust refractive index spectra, *J. Aerosol Sci.*, 114, 327–341, 2017,
<https://doi.org/10.1016/j.jaerosci.2017.10.003>.
- Takemura, T., Egashira, M., Matsuzawa, K., Ichijo, H., O'ishi, R., and Abe-Ouchi, A.: A simulation of the global distribution and radiative forcing of soil dust aerosols at the Last Glacial Maximum, *Atmos. Chem. Phys.*, 9, 3061–3073, 2009,
<https://doi.org/10.5194/acp-9-3061-2009>.
- 610 Tanaka, T. Y., Aoki, T., Takahashi, H., Shibata, K., Uchiyama, A., and Mikami, M.: Study of the sensitivity of optical properties of mineral dust to the direct aerosol radiative perturbation using a global aerosol transport model, *SOLA*, 3, 33–36, 2007, <https://doi.org/10.2151/sola.2007-009>.
- Tegen, I. and Lacis, A.: Modeling of particle size distribution and its influence on the radiative properties of mineral dust aerosol, *J. Geophys. Res.*, 101, 19237–19244, 1996, <https://doi.org/10.1029/95JD03610>.
- 615 Toth III, J. R., Rajupet, S., Squire, H., Volbers, B., Zhou, J., Xie, L., Sankaran, R. M., and Lacks, D. J.: Electrostatic forces alter particle size distributions in atmospheric dust, *Atmos. Chem. Phys.*, 20, 3181–3190,
<https://doi.org/10.5194/acp-20-3181-2020>, 2020.



- Tuccella, P., Curci, G., Pitari, G., Lee, S., and Jo, D. S.: Direct radiative effect of absorbing aerosols: sensitivity to mixing state, brown carbon and soil dust refractive index and shape, *J. Geophys. Res.-Atmos.*, 125, e2019JD030967, 2020, <https://doi.org/10.1029/2019JD030967>.
- 620
- van der Does, M., Knippertz, P., Zschenderlein, P., Giles Harrison, R., and Stuut, J.-B. W.: The mysterious long-range transport of giant mineral dust particles, *Sci. Adv.*, 4, eaau2768, 2018, <https://doi.org/10.1126/sciadv.aau2768>.
- Volz, F.: Infrared optical constants of aerosols at some locations, *Appl. Optics*, 22, 23, 3690–3700, 1983, <https://doi.org/10.1364/AO.11.000755>.
- 625
- Wagner, R., Ajtai, T., Kandler, K., Lieke, K., Linke, C., Müller, T., Schnaiter, M., and Vragel, M.: Complex refractive indices of Saharan dust samples at visible and near UV wavelengths: a laboratory study, *Atmos. Chem. Phys.*, 12, 2491–2512, 2012, <https://doi.org/10.5194/acp-12-2491-2012>.
- Wan, Z., Hook, S., and Hulley, G.: MOD11C2 MODIS/Terra Land Surface Temperature/Emissivity 8-Day L3 Global 0.05Deg CMG V006 [Data set]. NASA EOSDIS Land Processes DAAC, 2015, <https://doi.org/10.5067/MODIS/MOD11C2.006>.
- 630
- Wiegner, M., Gasteiger, J., Kandler, K., Weinzierl, B., Rasp, K., Esselborn, M., Freudenthaler, V., Heese, B., Toledano, C., Tesche, M., and Althausen, D.: Numerical simulations of optical properties of Saharan dust aerosols with emphasis on lidar applications, *Tellus B*, 61, 180–194, 2009, <https://doi.org/10.1111/j.1600-0889.2008.00381.x>
- Xu, L. and Penner, J. E.: Global simulations of nitrate and ammonium aerosols and their radiative effects, *Atmos. Chem. Phys.*, 12, 9479–9504, 2012, <https://doi.org/10.5194/acp-12-9479-2012>.
- 635
- Yang, E.-S., Gupta, P., and Christopher, S. A.: Net radiative effect of dust aerosols from satellite measurements over Sahara, *Geophys. Res. Lett.*, 36, L18812, 2009, <https://doi.org/10.1029/2009GL039801>
- Yoshioka, M., Mahowald, N., Conley, A. J., Collins, W. D., Fillmore, D.W., Zender, C. S., and Coleman, D. B.: Impact of desert dust radiative forcing on Sahel precipitation: relative importance of dust compared to sea surface temperature variations, vegetation changes and greenhouse gas warming, *J. Climate*, 16, 1445–1467, 2007, <https://doi.org/10.1175/JCLI4056.1>.
- 640



- Zhang, D., and Iwasaka, Y.: Size change of Asian dust particles caused by sea salt interaction: Measurements in southwestern Japan, *Geophys. Res. Lett.*, 31, L15102, 2004, <https://doi.org/10.1029/2004GL020087>.
- Zhang, J. and Christopher, S. A.: Longwave radiative forcing of Saharan dust aerosols estimated from MODIS, MISR, and CERES observations on Terra, *Geophys. Res., Lett.*, 30(23), 2188, 2003, <https://doi.org/10.1029/2003GL018479>
- 645 Zhao, C., Chen, S., Leung, L. R., Qian, Y., Kok, J. F., Zaveri, R. A., and Huang, J.: Uncertainty in modeling dust mass balance and radiative forcing from size parameterization, *Atmos. Chem. Phys.*, 13, 10733–10753, 2013, <https://doi.org/10.5194/acp-13-10733-2013>.
- Zhou, Y., Levy, R. C., Remer, L. A., Mattoo, S., and Espinosa, W. R.: Dust aerosol retrieval over the oceans with the MODIS/VIIRS dark target algorithm: 2. Nonspherical dust model, *Earth Space Sci.*, 7, e2020EA001222, 2020, <https://doi.org/10.1029/2020EA001222>.
- 650



Figure captions

Figure 1. Imaginary part of the refractive index at a wavelength of 0.52 and 9.7 μm for the nine main source regions and the global mean for others. The refractive index obtained from 19 samples was aggregated into 9 main source regions and the arithmetic mean was calculated for each source region (Di Biagio et al., 2017, 2019). The
655 coordinates of the nine source regions were: (1) western North Africa ($20^{\circ}\text{W} - 7.5^{\circ}\text{E}$; $18^{\circ}\text{N} - 37.5^{\circ}\text{N}$), (2) eastern North Africa ($7.5^{\circ}\text{E} - 35^{\circ}\text{E}$; $18^{\circ}\text{N} - 37.5^{\circ}\text{N}$), (3) the Sahel ($20^{\circ}\text{W} - 35^{\circ}\text{E}$; $0^{\circ}\text{N} - 18^{\circ}\text{N}$), (4) Middle East / Central Asia ($30^{\circ}\text{E} - 70^{\circ}\text{E}$ for $0^{\circ}\text{N} - 35^{\circ}\text{N}$, and $30^{\circ}\text{E} - 75^{\circ}\text{E}$ for $35^{\circ}\text{N} - 50^{\circ}\text{N}$), (5) East Asia ($70^{\circ}\text{E} - 120^{\circ}\text{E}$; $35^{\circ}\text{N} - 50^{\circ}\text{N}$), (6) North America ($130^{\circ}\text{W} - 80^{\circ}\text{W}$; $20^{\circ}\text{N} - 45^{\circ}\text{N}$), (7) Australia ($110^{\circ}\text{E} - 160^{\circ}\text{E}$; $10^{\circ}\text{S} - 40^{\circ}\text{S}$), (8) South America
660 ($80^{\circ}\text{W} - 20^{\circ}\text{W}$; $0^{\circ}\text{S} - 60^{\circ}\text{S}$), and (9) Southern Africa ($0^{\circ}\text{E} - 40^{\circ}\text{E}$; $0^{\circ}\text{S} - 40^{\circ}\text{S}$).

Figure 2. Model-simulated dust loads at fine (smaller than 2.5 μm of diameter) and coarse size ranges (larger than 2.5 μm of diameter) before and after adjusting the size-resolved dust load with DustCOMM. Results were shown for (a) fine dust from DustCOMM, (b) fine dust from default, (c) fine dust from improved, (d) coarse dust from DustCOMM, (e) coarse dust from default and (f) coarse dust from improved simulations. The parentheses
665 represented the global dust burden (T_g). The values of dust load at each bin were listed in Table 3.

Figure 3. The model better reproduced semi-observation-based data of DAOD_{550} in boreal summer (June, July, and August) after considering the dust asphericity. (a) semi-observation-based estimates of the DAOD_{550} were averaged over 2004–2008 (Ridley et al., 2016; Adebisi et al., 2020). The model results were shown for (b) default, (c) improved, and (d) fine-global simulations. The values of DAOD_{550} at the 15 regions (marked in Fig. 3a) in summer
670 were listed in Table S1. The scatter plot was shown in Fig. S1. The summer season was shown because most semi-observation-based data on dust radiative effects were available. The comparison for other seasons was presented in Table S2.

Figure 4. Summertime dust SW radiative effect efficiency. Semi-observation-based data at (a) the surface and (b) TOA were based on satellite observations (Yang et al. 2009; Li et al., 2004; Song et al., 2018; Christopher and Jones, 2007). The model results were shown for (c) and (d) default, and (e) and (f) improved simulations at the
675 surface and TOA, respectively. The regionally averaged values were listed in Tables S3 and S4 at the surface and



TOA, respectively. The scatter plot was shown in Fig. S2. The results from other sensitivity simulations were also shown in Fig. S3.

680 Figure 5. Summertime dust LW radiative effect efficiency. Semi-observation-based estimates at (a) surface and (b) TOA were based on satellite observations (Song et al., 2018; Christopher and Jones, 2007; Zhang and Christopher, 2003; Brindley and Russell, 2009; Yang et al., 2009). The model results were shown for (c) and (d) default, and (e) and (f) improved simulations at the surface and TOA, respectively. The regionally averaged values were listed in Tables S5 and S6 at the surface and TOA, respectively. The scatter plot was shown in Fig. S4. The results from other sensitivity simulations were also shown in Fig. S5.

685 Figure 6. Dust SW radiative effect ($\text{W}\cdot\text{m}^{-2}$) and radiative heating of the atmosphere (i.e., the subtraction of radiative effects from TOA to the surface in unit of $\text{W}\cdot\text{m}^{-2}$). The model results were shown for the simulations for (a) default at the surface, (b) improved at the surface, (c) default in atmospheric column, (d) improved in atmospheric column, (e) default at TOA, and (f) improved simulations at TOA. The numbers in parentheses represented the global mean.

690 Figure 7. Dust LW radiative effect ($\text{W}\cdot\text{m}^{-2}$) and radiative heating of the atmosphere (i.e., the subtraction of radiative effects from TOA to the surface in unit of $\text{W}\cdot\text{m}^{-2}$). The model results were shown for the simulations for (a) default at the surface, (b) improved at the surface, (c) default in atmospheric column, (d) improved in atmospheric column, (e) default at TOA, and (f) improved simulations at TOA. The numbers in parentheses represented the global mean.

695 Figure 8. Dust radiative effect ($\text{W}\cdot\text{m}^{-2}$) and radiative heating of the atmosphere (i.e., the subtraction of radiative effects from TOA to the surface in unit of $\text{W}\cdot\text{m}^{-2}$). The model results were shown for the simulations for (a) default at the surface, (b) improved at the surface, (c) default in atmospheric column, (d) improved in atmospheric column, (e) default at TOA, and (f) improved simulations at TOA. The numbers in parentheses represented the global mean.

700 Figure 9. Radiative effect ($\text{W}\cdot\text{m}^{-2}$) of mineral dust due to various aerosol absorptivity at the surface and TOA for (a) total dust SW, (b) total dust LW, and (c) total dust NET. The annually averaged values were listed in Table 5. The dashed line represented a 1 : 1 correspondence and corresponded to no change in radiative heating within the atmosphere.



Table 1. Summary of seven simulations compared in this study.

Experiment	Simulation	Size-resolved dust	Sphericity	SW refractive index	LW refractive index
Experiment 1	Default	IMPACT	Spherical	Mineralogical map ^d	Di Biagio et al. (2017)
Experiment 2 ^a	Improved	DustCOMM ^b	Aspherical ^c	Di Biagio et al. (2019)	Volz (1983)
Experiment 3	Fine-global	IMPACT	Aspherical ^c	Di Biagio et al. (2019)	Di Biagio et al. (2017)
Experiment 4	Coarse-global	DustCOMM ^b	Aspherical ^c	Di Biagio et al. (2019)	Di Biagio et al. (2017)
Experiment 5	Coarse-region	DustCOMM ^b	Aspherical ^c	Regional mean ^e	Regional mean ^e
Experiment 6	Coarse-mineral	DustCOMM ^b	Aspherical ^c	Mineralogical map ^d	Volz (1983)
Experiment 7	Coarse-absorption	DustCOMM ^b	Aspherical ^c	Less SW ^f	More LW ^g

^aCombination of coarse-global (Experiment 4) for SW and coarse-mineral (Experiment 6) for LW.

^bSize-resolved dust concentration was adjusted with semi-observation-based estimate (Adebiyi & Kok, 2020).

^cDust asphericity was considered in calculating the refractive index, which further assumed internal mixing of minerals (Huang et al., 2020b) using a volume-weighted mixture for each size bin.

^dMineralogical composition of dust aerosol for each size was prescribed at emission by mineralogical map (Journet et al., 2014; Ito and Shi 2016). The more absorptive SW refractive indices (Bedidi and Cervelle, 1993; Stegmann & Yang, 2017; Long et al., 1993) were used for mineral dust, compared to the less absorptive global mean data set (Di Biagio et al., 2019).

^eRegional mean of refractive index was calculated for the nine main source regions (Fig. 1). The global mean was used for other areas.

^fLess absorptive SW refractive indices were calculated by varying the values of the imaginary parts of the refractive index within the range of values from Di Biagio et al. (2019) (10% percentile).

^gMore absorptive LW refractive indices were calculated by varying the values of the imaginary parts of the refractive index within the range of values from Di Biagio et al. (2017) (90% percentile).



Table 2. Summary of radiative effects estimated in this study.

SW radiative effect	LW radiative effect	Difference
Less absorptive SW, coarser particle size, & aspherical shape	More absorptive LW, coarser particle size, & aspherical shape	Experiment 2 – Experiment 1
Less absorptive SW & aspherical shape	Aspherical shape	Experiment 3 – Experiment 1
Size-resolved dust abundance	Size-resolved dust abundance	Experiment 3 – Experiment 4
Regional variability in refractive index	Regional variability in refractive index	Experiment 5 – Experiment 4
Mineralogical variability in refractive index (more absorptive SW)	Mineralogical variability in refractive index (more absorptive LW)	Experiment 6 – Experiment 4
Less absorptive SW (10% percentile)	More absorptive LW (90% percentile)	Experiment 7 – Experiment 4



Table 3. Annually averages of dust load (Tg), mass extinction efficiency ($\text{m}^2 \text{g}^{-1}$), and DAOD_{50} at each bin on a global scale. The size-resolved dust concentration and shape in default simulation was adjusted to DustCOMM in improved simulation. At the same time, we maintained the consideration of asphericity on the gravitational velocity and kept the dust concentrations unaltered between the default and fine-global simulations.

Dust size bin	Dust load				Mass extinction efficiency				DAOD_{50}						
	Default	Improved	DustCOMM	Default	Improved	Fine-global	DustCOMM	Default	Improved	Fine-global	DustCOMM	Default	Improved	Fine-global	DustCOMM
Bin 1*	1.2	0.8	1.2 ± 0.7	2.11	3.41	3.33	3.06	0.0050	0.0055	0.0078	0.0070	0.0050	0.0055	0.0078	0.0070
Bin 2 (1.26–2.5 μm)	4.7	2.6	3.5 ± 2.1	0.73	1.25	1.21	1.22	0.0067	0.0064	0.0111	0.0084	0.0067	0.0064	0.0111	0.0084
Bin 3 (2.5–5 μm)	8.2	6.2	6.8 ± 3.8	0.37	0.59	0.57	0.57	0.0060	0.0071	0.0092	0.0077	0.0060	0.0071	0.0092	0.0077
Bin 4 (5–20 μm)	10.9	22.2	16.8 ± 9.0	0.23	0.24	0.29	0.19	0.0050	0.0104	0.0063	0.0063	0.0050	0.0104	0.0063	0.0063
Sum of 4 bins	25.0	31.8	28.4 ± 15.5	0.46	0.47	0.70	0.53	0.0227	0.0295	0.0345	0.0294	0.0227	0.0295	0.0345	0.0294

*Bin 1 in the default model is 0.1–1.26 μm , whereas bin 1 in the improved model and DustCOMM is 0.2–1.26 μm .



Table 4. Semi-observation-based data set of clear-sky dust radiative effect efficiency at the surface and TOA.

Number	Region name	Season	Region coordinates	Aerosol type selection	AOD data
1 ^a	Sahara Desert	Summer	15°–30°N, 10°W–30°E	No selection	OMI-MISR
2 ^b	Tropical Atlantic	Summer	15°–25°N, 45°–15°W	MODIS effective radius peaks 0.8–0.9 μm	MODIS
3 ^c	Tropical Atlantic	Summer	10°–30°N, 45°–20°W	CALJOP dust and polluted dust	CERES-CALIPSO-CloudSat-MODIS
4 ^d	Atlantic Ocean	Summer	0°–30°N, 60°–10°W	Dust detection based on DAOD ₅₅₀ and fraction	MODIS
5 ^{e,f}	North Africa	Summer	15°–35°N, 18°W–40°E	No selection	MISR ^e or SEVIRI ^f
6 ^{e,f}	West Africa	Summer	16°–28°N, 16°–4°W	No selection	MISR ^e or SEVIRI ^f
7 ^{e,f}	Niger-Chad	Summer	15°–20°N, 15°–22°E	No selection	MISR ^e or SEVIRI ^f
8 ^{e,f}	Sudan	Summer	15°–22°N, 22°–36°E	No selection	MISR ^e or SEVIRI ^f
9 ^{e,f}	Egypt-Israel	Summer	23°–32°N, 23°–35°E	No selection	MISR ^e or SEVIRI ^f
10 ^{e,f}	North Libya	Summer	27°–33°N, 15°–25°E	No selection	MISR ^e or SEVIRI ^f
11 ^{e,f}	South Libya	Summer	23°–27°N, 15°–25°E	No selection	MISR ^e or SEVIRI ^f
12 ^g	Mediterranean	Summer	35.5°N, 12.6°E	Dust detection based on optical property	Ground-based measurements
13 ^h	Cape Verde	Summer	16.7°N, 22.9°E	Dust detection based on brightness temperature	Ground-based measurements
14 ⁱ	China	Spring	39°N, 101°E	Dust detection based on brightness temperature	Ground-based measurements

^aYang et al. (2009). ^bLi et al. (2004). ^cSong et al. (2018). ^dChristopher and Jones (2007). ^eZhang and Christopher (2003). ^fBrindley and Russell (2009). ^gDi Biagio et al. (2010). ^hHansell et al. (2010). ⁱHansell et al. (2012).



Table 5. Annually averages of short-wave (SW) ($\text{W}\cdot\text{m}^{-2}$), long-wave (LW) ($\text{W}\cdot\text{m}^{-2}$), and net radiative effect (NET) ($\text{W}\cdot\text{m}^{-2}$) at the surface, TOA, and atmospheric radiative heating on a global scale.

Data	Total dust SW			Total dust LW			Total dust NET			Fine dust NET			Coarse dust NET		
	TOA (surface)	Atmosphere	Atmosphere	TOA (surface)	Atmosphere	Atmosphere	TOA (surface)	Atmosphere	Atmosphere	TOA (surface)	Atmosphere	Atmosphere	TOA (surface)	Atmosphere	Atmosphere
Default	-0.18 (-1.3)	1.07	+0.09 (0.37)	-0.29	-0.09 (-0.88)	0.79	-0.23 (-0.52)	0.29	+0.14 (-0.33)	0.47					
Improved	-0.32 (-1.2)	0.91	+0.23 (1.00)	-0.77	-0.08 (-0.23)	0.15	-0.22 (-0.29)	0.07	+0.16 (+0.05)	0.10					
Fine-global	-0.49 (-1.3)	0.86	+0.12 (0.50)	-0.38	-0.37 (-0.84)	0.48	-0.35 (-0.53)	0.17	+0.02 (-0.28)	0.30					
Course-global	-0.32 (-1.2)	0.91	+0.11 (0.58)	-0.46	-0.20 (-0.65)	0.45	-0.24 (-0.33)	0.09	+0.06 (-0.30)	0.36					
Course-region	-0.33 (-1.2)	0.87	+0.11 (0.53)	-0.43	-0.23 (-0.67)	0.44	-0.24 (-0.33)	0.10	+0.04 (-0.31)	0.34					
Course-mineral	+0.02 (-1.6)	1.63	+0.23 (1.00)	-0.77	+0.25 (-0.62)	0.87	-0.12 (-0.38)	0.26	+0.38 (-0.22)	0.60					
Course-absorption	-0.54 (-1.0)	0.43	+0.16 (0.76)	-0.60	-0.38 (-0.22)	-0.16	-0.26 (-0.25)	-0.01	-0.08 (+0.03)	-0.11					
DustCOMM	-0.43 ± 0.21		+0.32 ± 0.08		-0.11 ± 0.10		-0.33 ± 0.16		+0.24 ± 0.11						

The parentheses represent the RE at the surface. The bold represents the combination of course-global for SW and course-mineral for LW (i.e., improved simulation).

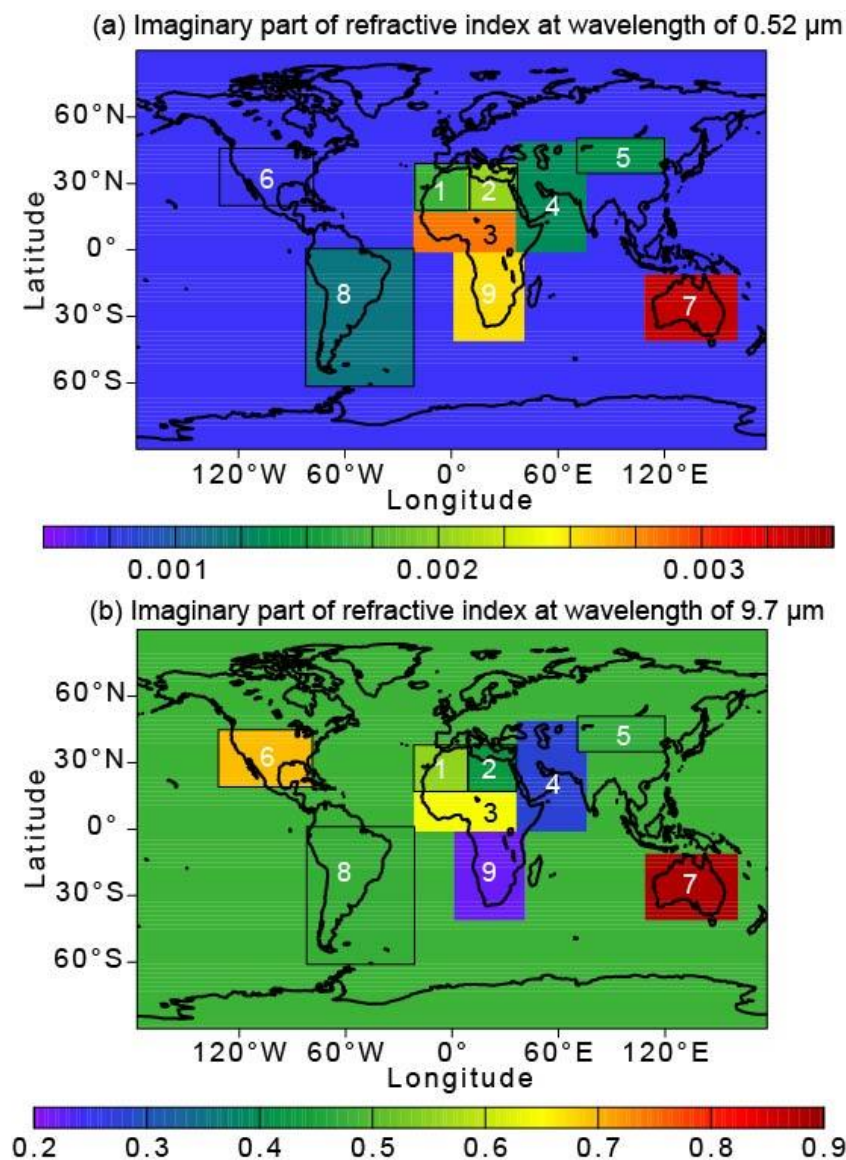


Figure 1. Imaginary part of the refractive index at a wavelength of 0.52 and 9.7 μm for the nine main source regions

and the global mean for others. The refractive index obtained from 19 samples was aggregated into 9 main source regions

710 and the arithmetic mean was calculated for each source region (Di Biagio et al., 2017, 2019). The coordinates of the nine
source regions were: (1) western North Africa (20°W – 7.5°E; 18°N – 37.5°N), (2) eastern North Africa (7.5°E – 35°E; 18°N
– 37.5°N), (3) the Sahel (20°W – 35°E; 0°N – 18°N), (4) Middle East / Central Asia (30°E – 70°E for 0°N – 35°N, and 30°E
– 75°E for 35°N – 50°N), (5) East Asia (70°E – 120°E; 35°N – 50°N), (6) North America (130°W – 80°W; 20°N – 45°N),
(7) Australia (110°E – 160°E; 10°S – 40°S), (8) South America (80°W – 20°W; 0°S – 60°S), and (9) Southern Africa (0°E –
715 40°E; 0°S – 40°S).

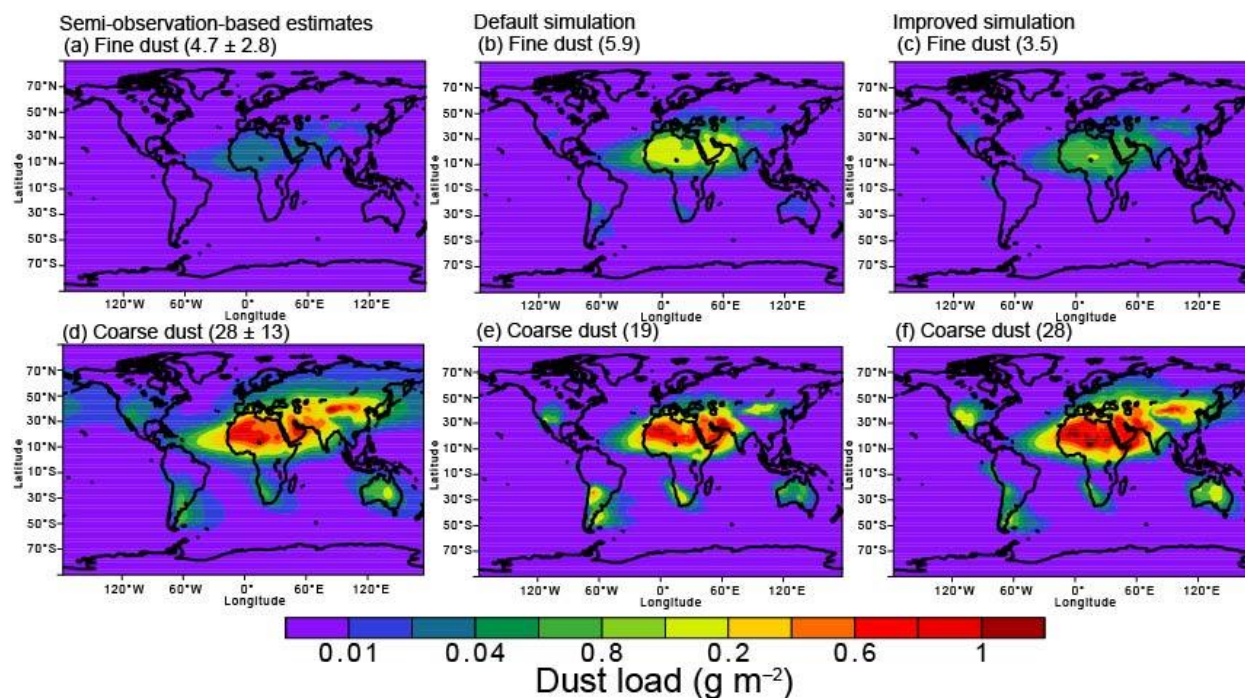
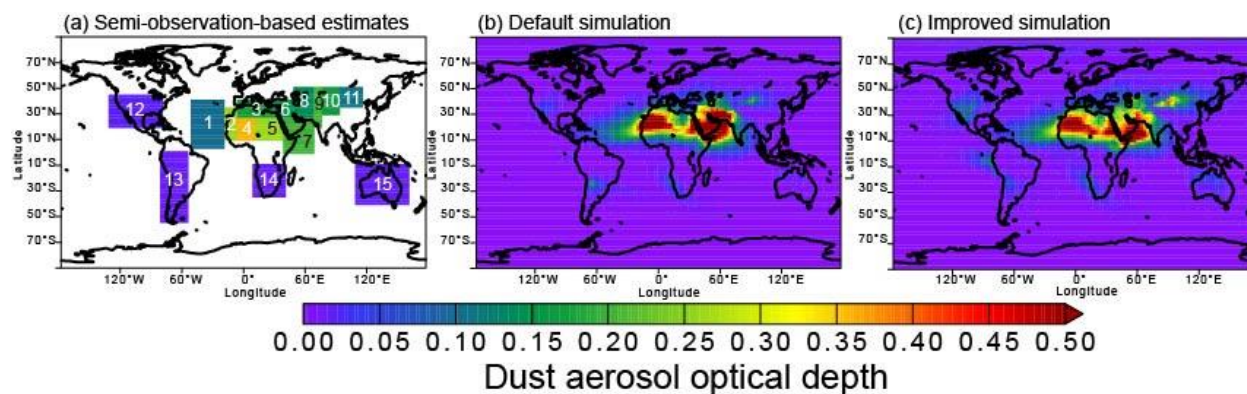


Figure 2. Model-simulated dust loads at fine (smaller than 2.5 μm of diameter) and coarse size ranges (larger than 2.5 μm of diameter) before and after adjusting the size-resolved dust load with DustCOMM. Results were shown for (a) fine dust from DustCOMM, (b) fine dust from default, (c) fine dust from improved, (d) coarse dust from DustCOMM, (e) coarse dust from default and (f) coarse dust from improved simulations. The parentheses represented the global dust burden (Tg). The values of dust load at each bin were listed in Table 3.



725 **Figure 3.** The model better reproduced semi-observation-based data of DAOD₅₅₀ in boreal summer (June, July, and August) after considering the dust asphericity. (a) semi-observation-based estimates of the DAOD₅₅₀ were averaged over 2004–2008 (Ridley et al., 2016; Adebisi et al., 2020). The model results were shown for (b) default, (c) improved, and (d) fine-global simulations. The values of DAOD₅₅₀ at the 15 regions (marked in Fig. 3a) in summer were listed in Table S1. The scatter plot was shown in Fig. S1. The summer season was shown because most semi-observation-based data on dust
730 radiative effects were available. The comparison for other seasons was presented in Table S2.

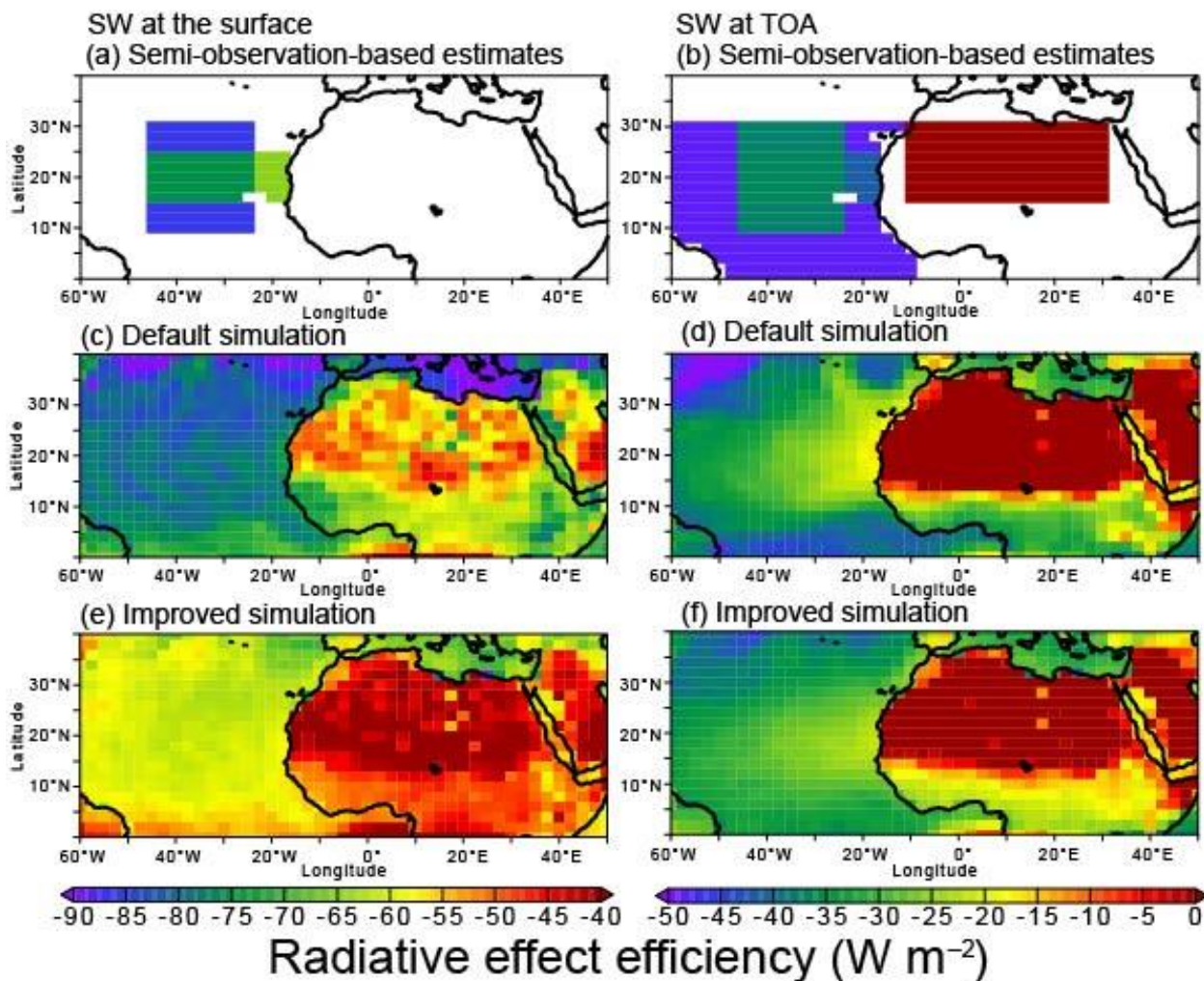
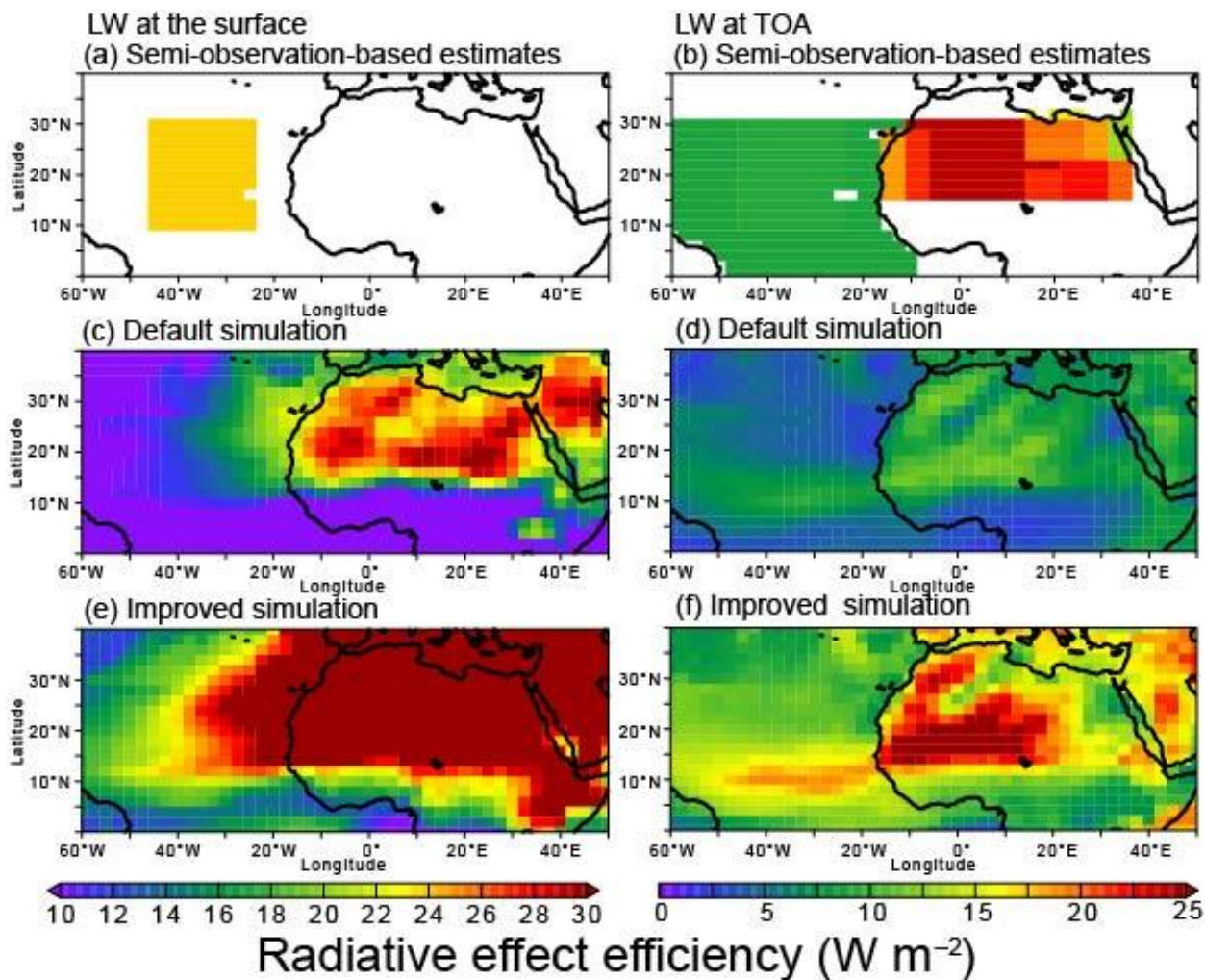


Figure 4. Summertime dust SW radiative effect efficiency. Semi-observation-based data at (a) the surface and (b) TOA were based on satellite observations (Yang et al. 2009; Li et al., 2004; Song et al., 2018; Christopher and Jones, 2007). The model results were shown for (c) and (d) default, and (e) and (f) improved simulations at the surface and TOA, respectively. The regionally averaged values were listed in Tables S3 and S4 at the surface and TOA, respectively. The scatter plot was shown in Fig. S2. The results from other sensitivity simulations were also shown in Fig. S3.



740 **Figure 5.** Summertime dust LW radiative effect efficiency. Semi-observation-based estimates at (a) surface and (b)
745 TOA were based on satellite observations (Song et al., 2018; Christopher and Jones, 2007; Zhang and Christopher, 2003;
Brindley and Russell, 2009; Yang et al., 2009). The model results were shown for (c) and (d) default, and (e) and (f)
improved simulations at the surface and TOA, respectively. The regionally averaged values were listed in Tables S5 and S6
at the surface and TOA, respectively. The scatter plot was shown in Fig. S4. The results from other sensitivity simulations
were also shown in Fig. S5.

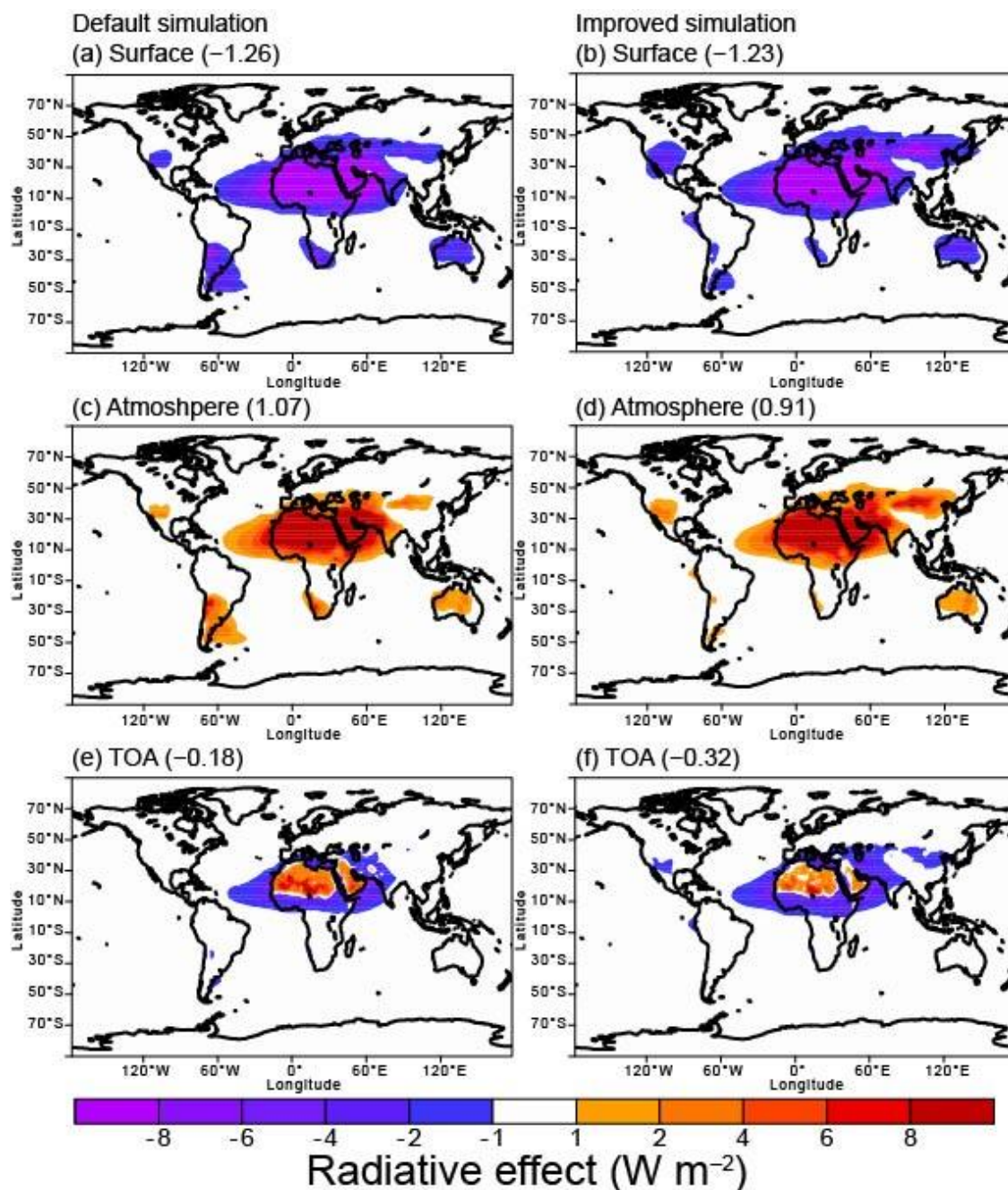
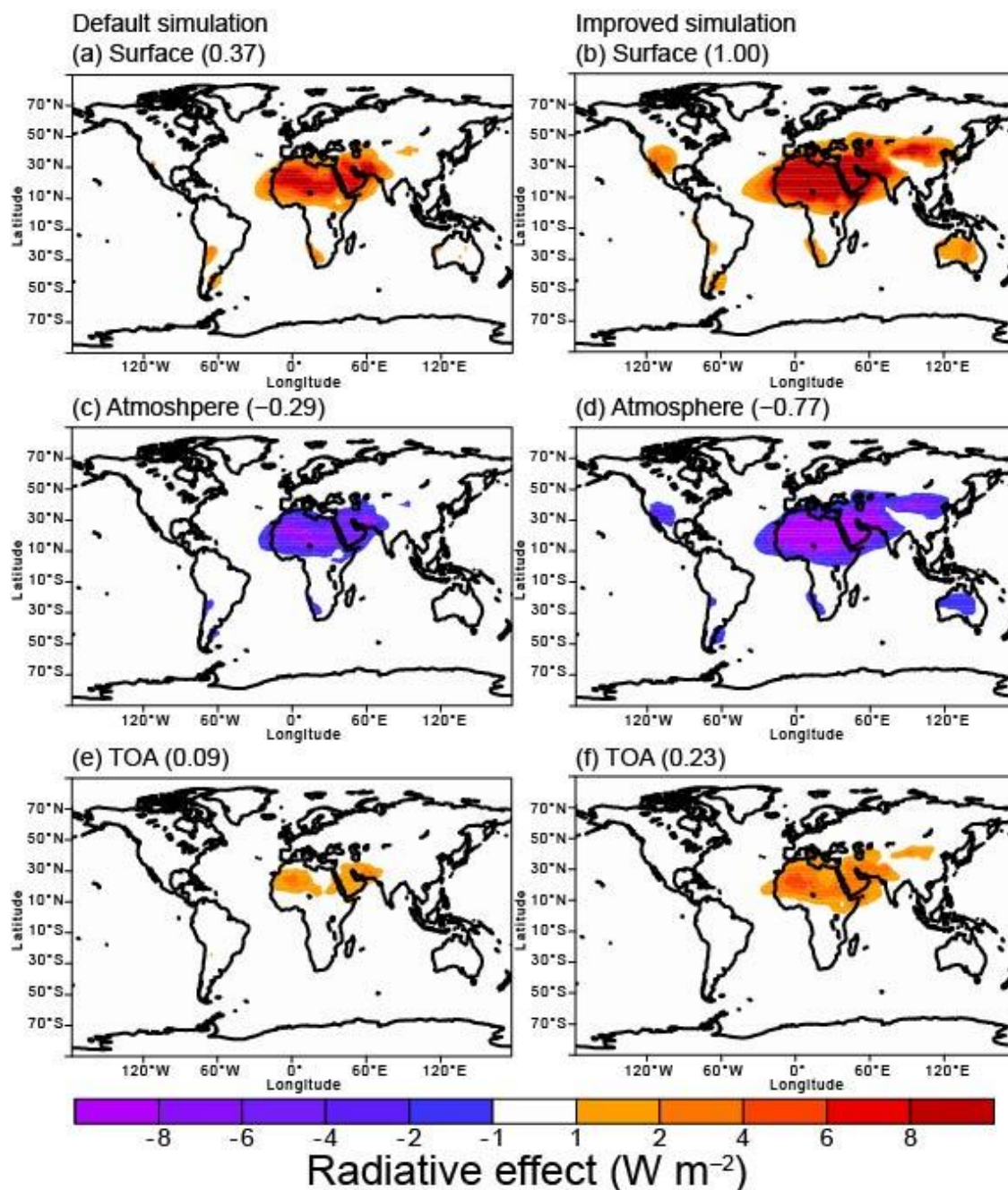


Figure 6. Dust SW radiative effect ($\text{W} \cdot \text{m}^{-2}$) and radiative heating of the atmosphere (i.e., the subtraction of radiative effects from TOA to the surface in unit of $\text{W} \cdot \text{m}^{-2}$). The model results were shown for the simulations for (a) default at the surface, (b) improved at the surface, (c) default in atmospheric column, (d) improved in atmospheric column, (e) default at TOA, and (f) improved simulations at TOA. The numbers in parentheses represented the global mean.



755 **Figure 7.** Dust LW radiative effect ($\text{W}\cdot\text{m}^{-2}$) and radiative heating of the atmosphere (i.e., the subtraction of radiative effects from TOA to the surface in unit of $\text{W}\cdot\text{m}^{-2}$). The model results were shown for the simulations for (a) default at the surface, (b) improved at the surface, (c) default in atmospheric column, (d) improved in atmospheric column, (e) default at TOA, and (f) improved simulations at TOA. The numbers in parentheses represented the global mean.

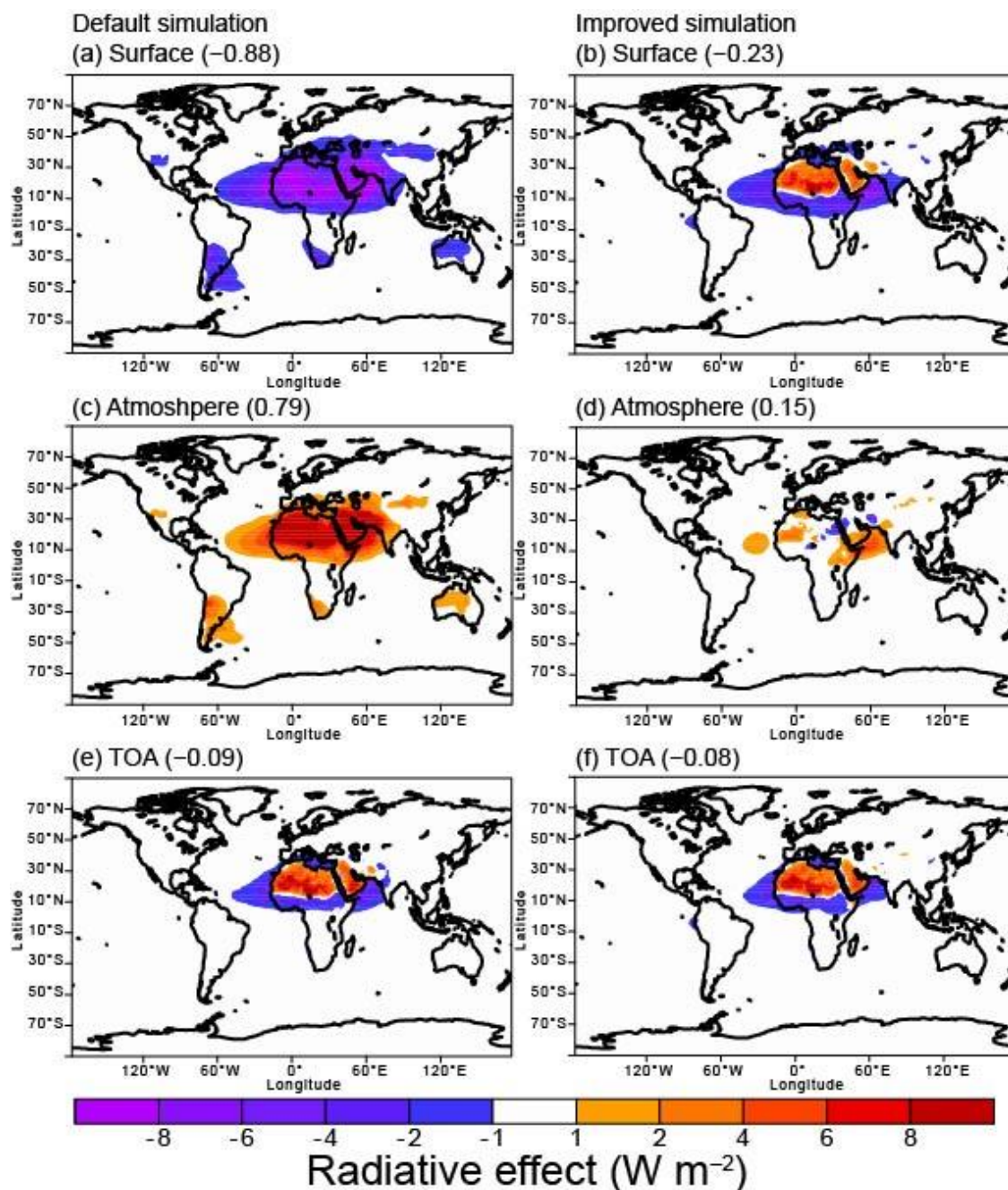
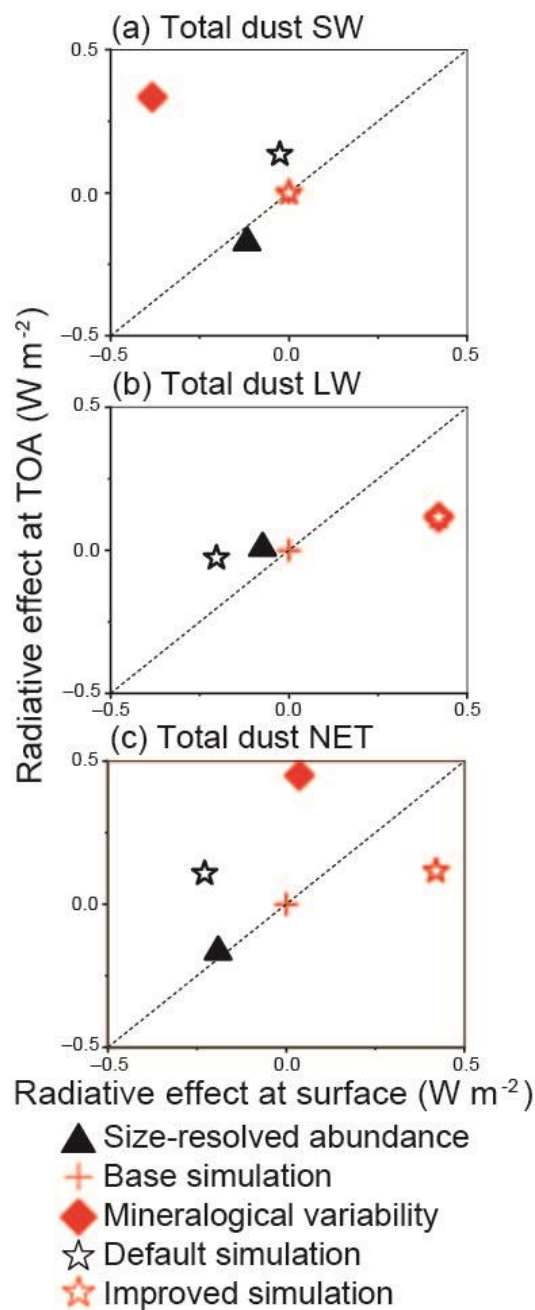


Figure 8. Dust radiative effect (W m^{-2}) and radiative heating of the atmosphere (i.e., the subtraction of radiative effects from TOA to the surface in unit of W m^{-2}). The model results were shown for the simulations for (a) default at the surface, (b) improved at the surface, (c) default in atmospheric column, (d) improved in atmospheric column, (e) default at TOA, and (f) improved simulations at TOA. The numbers in parentheses represented the global mean.



765 **Figure 9.** Radiative effect ($\text{W} \cdot \text{m}^{-2}$) of mineral dust due to various aerosol absorptivity at the surface and TOA for (a) total dust SW, (b) total dust LW, and (c) total dust NET. The annually averaged values were listed in Table 5. The dashed line represented a 1 : 1 correspondence and corresponded to no change in radiative heating within the atmosphere.